The mTOR pathway genes *mTOR*, *Rheb*, *Depdc5*, *Pten*, and *Tsc1* have convergent and divergent impacts on cortical neuron development and function

Lena H. Nguyen[1, 2*], Youfen Xu[2], Maanasi Nair[2], Angelique Bordey[2*]

Author affiliations:

[1]Department Neuroscience, School of Behavioral and Brain Sciences, University of Texas at Dallas, Richardson, TX 75080, USA

[2]Departments of Neurosurgery and Cellular & Molecular Physiology, Wu Tsai Institute, Yale University School of Medicine, New Haven, CT 06510, USA

*Co-corresponding authors:

Lena H. Nguyen, Ph.D.

Email: lena.nguyen@utdallas.edu

Angelique Bordey, Ph.D.

Email: angelique.bordey@yale.edu

ABSTRACT

Brain somatic mutations in various components of the mTOR complex 1 (mTORC1) pathway have emerged as major causes of focal malformations of cortical development and intractable epilepsy. While these distinct gene mutations converge on excessive mTORC1 signaling and lead to common clinical manifestations, it remains unclear whether they cause similar cellular and synaptic disruptions underlying cortical network hyperexcitability. Here, we show that *in utero* activation of the mTORC1 activators, *Rheb* or *mTOR*, or biallelic inactivation of the mTORC1 repressors, *Depdc5*, *Tsc1*, or *Pten* in mouse medial prefrontal cortex leads to shared alterations in pyramidal neuron morphology, positioning, and membrane excitability but different changes in excitatory synaptic transmission. Our findings suggest that, despite converging on mTORC1 signaling, mutations in different mTORC1 pathway genes differentially impact cortical excitatory synaptic activity, which may confer gene-specific mechanisms of hyperexcitability and responses to therapeutic intervention.

Keywords: malformation of cortical development, epilepsy, seizures, HCN4, resting membrane potential, action potential, synaptic activity.

INTRODUCTION

Focal malformations of cortical development (FMCDs), including focal cortical dysplasia type II (FCDII) and hemimegalencephaly (HME), are the most common causes of intractable epilepsy in children[1,2]. These disorders are characterized by abnormal brain cytoarchitecture with cortical overgrowth, mislamination, and cellular anomalies, and are often associated with developmental delay and intellectual disability[3]. Early immunohistochemical studies identified hyperactivation of the mechanistic target of rapamycin complex 1 (mTORC1) signaling pathway in resected brain tissue from individuals with FCDII and HME, leading to the classification of these disorders as "mTORopathies"[4]. More recently, somatic mutations in numerous regulators of the mTORC1 pathway were identified as the genetic causes of FCDII and HME[5-7]. Accumulating evidence shows that these mutations occur in a subset of dorsal telencephalic progenitor cells that give rise to excitatory neurons during fetal development, resulting in brain somatic mosaicism[8,9]. These genetic findings provide opportunities for gene therapy approaches targeting the mTORC1 pathway for FCDII and HME.

mTORC1 is an evolutionarily conserved protein complex that promotes cell growth and differentiation through the regulation of protein synthesis, metabolism, and autophagy[10]. mTORC1 is composed of mTOR, a serine/threonine kinase that exerts the complex's catalytic function, and several companion proteins. Activation of mTORC1 is controlled by a well-described upstream cascade involving multiple protein regulators[11]. Stimulation by growth factors activates phosphoinositide 3-kinase (PI3K), which leads to the activation of phosphoinositide-dependent kinase 1 (PDK1) and subsequent phosphorylation and activation of AKT. Activated AKT phosphorylates and inactivates tuberous sclerosis complex 1/2 (TSC1/2 complex; consisting of TSC1 and TSC2 proteins), which releases the brake on Ras homolog enriched in brain (RHEB), a GTP-binding protein that directly activates mTORC1. This mTORC1-activating cascade is negatively controlled by the phosphatase and tensin homolog (PTEN) protein, which inhibits PI3K activation of PDK1. Additionally, mTORC1 signaling is regulated by a separate nutrient-sensing GAP Activity Towards Rags 1 *(*GATOR1) complex, which consists of DEP domain containing 5 (DEPDC5) and the nitrogen permease regulator 2-like (NPRL2) and 3-like (NPRL3) proteins[12]. The GATOR1 complex serves as a negative regulator of mTORC1 that inhibits mTORC1 at low amino acid levels.

Pathogenic mutations in numerous regulators that activate mTORC1 signaling, including *PIK3CA*, *PTEN*, *AKT3*, *TSC1*, *TSC2*, *MTOR*, *RHEB*, *DEPDC5*, *NPRL2*, and *NPRL3*, have been identified in HME and FCDII[9]. Genetic targeting of these genes in mouse models consistently recapitulates the epilepsy phenotype, supporting an important role for these genes in seizure generation[13,14]. However, while all these genes impinge on the mTORC1 pathway, many of them also participate in mTORC1-independent functions through parallel signaling pathways[13,15-19], and it is unclear whether mutations affecting different mTORC1 pathway genes lead to cortical hyperexcitability through common neural mechanisms. In this study, we examined how disruption of five distinct mTORC1 pathway genes, *Rheb*, *mTOR*, *Depdc5*, *Pten*, and *Tsc1*, individually impact pyramidal neuron development and electrophysiological function in the mouse medial prefrontal cortex (mPFC). Collectively, we found that activation of the mTORC1 activators, *Rheb* and *mTOR*, or inactivation of the mTORC1 repressors, *Depdc5*, *Tsc1*, and *Pten*, largely leads to similar alterations in neuron morphology and membrane excitability but differentially impacts excitatory synaptic activity. The latter has implications for cortical network function and seizure vulnerability and may affect how individuals with different genotypes respond to targeted therapeutics.

RESULTS

Expression of *Rheb*^{Y35L}, *mTOR*^{S2215Y}, *Dedpdc5*^{KO}, *Pten*^{KO}, and *Tsc1*^{KO} leads to varying magnitudes of neuronal enlargement and mispositioning in the cortex

To model somatic gain-of-function mutations in the mTORC1 activators, we individually expressed plasmids encoding *Rheb*^{Y35L} or *mTOR*^{S2215Y}, respectively, in select mouse neural progenitor cells during late corticogenesis via *in utero* electroporation (IUE) (**Fig. 1a, b**). These pathogenic variants were previously detected in brain tissue from children with FCDII and HME associated with intractable seizures[20-25]. We specifically targeted a subset of late-born progenitor cells that generate excitatory pyramidal neurons destined to layer 2/3 in the medial prefrontal cortex (mPFC) to mimic frontal lobe somatic mutations and the genetic mosaicism characteristic of these lesions. To model the somatic loss-of-function mutations in mTORC1 repressors, we expressed plasmids encoding previously validated CRISPR/Cas9 guide RNAs against *Depdc5*[26], *Tsc1*[27], or *Pten*[28] to individually knockout (KO) the respective genes using the same IUE approach (**Fig. 1a, b**). As a control for the activating mutations, we expressed plasmids encoding fluorescent

proteins under the same CAG promoter. As a control for the CRISPR/Cas9-mediated knockouts, we used an empty CRISPR/Cas9 vector containing no guide RNA sequences. To verify that the expression of these plasmids leads to mTORC1 hyperactivation, we assessed the phosphorylated levels of S6 (i.e., p-S6), a downstream substrate of mTORC1, using immunostaining in brain sections from postnatal day (P) 28-43 mice. As expected, we found that expression of the *Rheb*^{Y35L}, *mTOR*^{S2215Y}, *Dedpdc5*^{KO}, *Pten*^{KO}, and *Tsc1*^{KO} plasmids all led to significantly increased p-S6 staining intensity, supporting that the expression of each of these plasmids leads to increased mTORC1 signaling (**Fig. 1c, d, Table 1, Fig. S1a**).

Considering the cytoarchitectural abnormalities associated with mTORC1 hyperactivation, we compared neuron soma size and positioning in the cortex following *in utero* activation of *Rheb* and *mTOR* and inactivation of *Depdc5*, *Pten*, and *Tsc1* in P28-43 mice. While all experimental conditions led to increased neuron soma size, the magnitude of the enlargement was dependent on the specific gene that was targeted (**Fig. 1c, e, Table 1. Fig. S1b**). In particular, expression of *Rheb*^{Y35L} and *mTOR*^{S2215Y} led to the largest soma size changes, with a >3-fold increase from control. Expression of *Pten*^{KO} led to a similarly large increase of 2.7-fold, while expression of *Dedpdc5*^{KO} and *Tsc1*^{KO} led to a 1.7 and 2.1-fold increase, respectively. The increase in the *Pten*^{KO} condition was significantly higher than both the *Dedpdc5*^{KO} and *Tsc1*^{KO} conditions, and the increase in the *Tsc1*^{KO} condition was significantly higher than the *Dedpdc5*^{KO} condition. Although the above analysis was performed at P28-43, the enlargement of neuron soma sizes was already detected by P7-9 (**Fig. S2a-c, Table S1**). In terms of neuronal positioning, all experimental conditions, except for *Pten*^{KO}, resulted in neuron misplacement (**Fig. 1f-h, Table 1**). The *Rheb*^{Y35L} and *mTOR*^{S2215Y} conditions led to the most severe phenotype: ~70-80% of the neurons were misplaced outside of layer 2/3 (**Fig. 1g**), with the mispositioned neurons evenly scattered across the deeper layers (**Fig. 1h**). For the *Dedpdc5*^{KO} and *Tsc1*^{KO} conditions, ~45-60% of the neurons were misplaced outside of layer 2/3 (**Fig. 1g**), with the mispositioned neurons found closer to layer 2/3 (**Fig. 1h**). Taken together, these studies show that the expression of *Rheb*^{Y35L}, *mTOR*^{S2215Y}, *Dedpdc5*^{KO}, *Pten*^{KO}, and *Tsc1*^{KO} leads to varying magnitudes of neuronal enlargement and mispositioning in the cortex. Of note, *Pten*^{KO} neurons, despite exhibiting a 2.7-fold increase in neuron soma size, were mostly correctly positioned in layer 2/3. These findings suggest that while all experimental conditions lead to increased soma size, not all lead to neuron mispositioning, suggesting defective migration and the subsequent impact on neuron positioning occur independently of cell size.

Expression of *Rheb*^{Y35L}, *mTOR*^{S2215Y}, *Dedpdc5*^{KO}, *Pten*^{KO}, and *Tsc1*^{KO} universally leads to decreased depolarization-induced excitability, but only *Rheb*^{Y35L}, *mTOR*^{S2215Y}, and *Tsc1*^{KO} expression leads to depolarized resting membrane potential

To elucidate the contribution of each experimental condition to the function of cortical neurons, we obtained whole-cell patch clamp recordings of layer 2/3 pyramidal neurons at P26-P51 (**Fig. 2a**). The *Rheb*^{Y35L} and *mTOR*^{S2215Y} conditions were compared to a control group expressing fluorescent proteins under the same CAG promoter. The *Dedpdc5*^{KO}, *Pten*^{KO}, and *Tsc1*^{KO} conditions were compared to a CRISPR/Cas9 empty vector control. Recordings of control and experimental conditions were alternated to match the animal ages.

Consistent with the changes in soma size (**Fig. 1c, e**), recorded neurons displayed increased membrane capacitance in all experimental conditions (**Fig. 2b, Table 1, Fig. S3a**). Neurons expressing the *mTOR*^{S2215Y} variant had a larger capacitance increase than those expressing the *Rheb*^{Y35L} variant. *Pten*^{KO} and *Tsc1*^{KO} neurons had similar increases in capacitance that were both larger than that of the *Depdc5*^{KO} neurons. All neurons across the experimental conditions also had increased resting membrane conductance in a pattern that followed that of the capacitance (**Fig. 2c, Table 1, Fig. S3b**). However, while *Rheb*^{Y35L}, *mTOR*^{S2215Y}, and *Tsc1*^{KO} expression led to depolarized resting membrane potential (RMP), *Dedpdc5*^{KO} and *Pten*^{KO} expression did not significantly affect the RMP (**Fig. 2d, Table 1, Fig. S3c**). To assess whether these changes impacted neuron intrinsic excitability, we examined the action potential (AP) firing response to depolarizing current injections. For all experimental conditions, neurons fired fewer APs for current injections above 100 pA compared to the respective control neurons (**Fig. 2e, f, Table 1**). This decrease in intrinsic excitability is reflected in the increased rheobase (i.e., the minimum current required to induce an AP) in all experimental conditions, with the *mTOR*^{S2215Y} and *Rheb*^{Y35L} conditions leading to the largest rheobase increases (**Fig. 2g, Table 1, Fig. S3d**). Collectively, these findings indicate that *Rheb*^{Y35L}, *mTOR*^{S2215Y}, and *Tsc1*^{KO} neurons display a decreased ability to generate APs upon depolarization despite having depolarized RMPs. In terms of firing pattern, neurons in all groups displayed a regular-spiking pattern with spike-frequency adaptation (**Fig. 2e**). However, while an initial spike doublet (with an interspike interval of 10-15 ms) was observed in the majority of control neurons, consistent with the expected firing pattern for layer 2/3 mPFC pyramidal neurons[29], this was observed in a smaller fraction of neurons in the experimental conditions [number of neurons displaying spike doublets: *Rheb*^{Y35L}: 4/23 (17%), *mTOR*^{S2215Y}: 7/28

(25%), *Dedpdc5*^{KO}: 11/27 (41%), *Pten*^{KO}: 21/28 (75%) - notably, 6 of the 21 doublets are parts of triplets, *Tsc1*^{KO}: 7/28 (25%), control: 24/26 (92%)]. There were no differences in the AP threshold across the conditions (**Fig. 2h, Table 1, Fig. S3e**). The AP peak amplitude was decreased in the *mTOR*^{S2215Y} and *Tsc1*^{KO} conditions (**Fig. 2i, Table 1, Fig. S3f**), while the AP half-width was decreased in the *Rheb*^{Y35L}, *mTOR*^{S2215Y,} and *Pten*^{KO} conditions (**Fig. 2j, Table 1, Fig. S3g**). Taken together, these findings show that various genetic conditions that activate the mTORC1 pathway universally lead to decreased depolarization-induced excitability in layer 2/3 pyramidal neurons, with gene-dependent changes in RMP and several AP properties.

Expression of *Rheb*^{Y35L}, *mTOR*^{S2215Y}, *Dedpdc5*^{KO}, *Pten*^{KO}, and *Tsc1*^{KO} leads to the abnormal presence of HCN4 channels with variations in functional expression

We recently reported that neurons expressing *Rheb*^{S16H}, an mTOR activating variant of Rheb, display abnormal expression of HCN4 channels[30,31]. These channels give rise to a hyperpolarization-activated cation current (I_h) that is normally absent in layer 2/3 pyramidal neurons[30,31]. The aberrant I_h, which has implications for neuronal excitability, preceded seizure onset and was detected by P8-12 in mice[30]. Rapamycin treatment starting at P1 and expression of constitutive active 4E-BP1, a translational repressor downstream of mTORC1, prevented and alleviated the aberrant HCN4 channel expression, respectively[30,31]. These findings suggest that the abnormal HCN4 channel expression is mTORC1-dependent. Given that all the experimental conditions in the present study led to increased mTORC1 activity, we investigated whether they also resulted in abnormal HCN4 channel expression. Immunostaining for HCN4 channels using previously validated antibodies[30] in brain sections from P28-43 mice revealed significantly increased HCN4 staining intensity in the electroporated neurons in all experimental conditions compared to the respective controls, which exhibited no HCN4 staining (**Fig 3a, b, Table 1, Fig. S4a**). The increased staining was evident in the ipsilateral cortex containing *mTOR*^{S2215Y} electroporated neurons and absent in the non-electroporated contralateral cortex (**Fig. S5a**). These data indicate the presence of aberrant HCN4 channel expression following *Rheb*^{Y35L}, *mTOR*^{S2215Y}, *Depdc5*^{KO}, *Pten*^{KO}, or *Tsc1*^{KO} expression in layer 2/3 pyramidal neurons.

To examine the functional impacts of the aberrant HCN4 channel expression, we examined I_h amplitudes in the various experimental conditions. To evoke I_h, we applied a series of 3 s-long hyperpolarizing voltage steps from -120 mV to -40 mV. Consistent with previous findings in

Rheb^{S16H} neurons[30,31], hyperpolarizing voltage pulses elicited significantly larger inward currents in all experimental conditions compared to their respective controls (**Fig. 3c, d, Table 1).** The *mTOR*^{S2215Y} condition displayed larger inward currents than the *Rheb*^{Y35L} condition, while the *Pten*^{KO} condition displayed the largest inward currents compared to the *Depdc5*^{KO} and *Tsc1*^{KO} conditions (**Fig. 3d**). These data were proportional to the changes in neuron soma size (**Fig. 1e, 2b**). The inward currents in *Rheb*^{S16H} neurons are thought to result from the activation of both inward-rectifier K+ (Kir) channels and HCN channels[30]. Kir-mediated currents activate fast whereas HCN-mediated currents, i.e., I_h, activate slowly during hyperpolarizing steps; therefore, to assess I_h amplitudes, we measured the difference between the instantaneous and steady-state currents at the beginning and end of the voltage pulses, respectively (i.e., ΔI)[32]. The resulting ΔI-voltage (V) curve revealed significantly larger I_h amplitudes in all experimental conditions (**Fig. 3e, Table 1**). To further isolate the I_h from Kir -mediated currents, we measured I_h amplitudes at -90 mV, near the reversal potential of Kir channels to eliminate Kir-mediated current contamination. At -90 mV, I_h amplitudes were significantly higher in the *mTOR*^{S2215Y} and *Tsc1*^{KO} conditions compared to controls (**Fig. 3f, Table 1, Fig. S4b**). Of note, although the *Depdc5*^{KO} and *Pten*^{KO} conditions did not display a significant increase in I_h amplitudes at -90 mV, 1 out of 28 *Depdc5*^{KO} neurons and 4 out of 27 *Pten*^{KO} neurons had I_h amplitudes that were 2-fold greater than the mean I_h amplitude of the *Tsc1*^{KO} condition. 6 out of 24 *Rheb*^{Y35L} neurons also had I_h amplitudes 2-fold greater than this value (**Fig. 3f**). These data suggest that I_h currents are present in a subset of *Rheb*^{Y35L}, *Depdc5*^{KO} , and *Pten*^{KO} neurons, and most *mTOR*^{S2215Y} and *Tsc1*^{KO} neurons.

Considering that the *mTOR*^{S2215Y} condition led to the largest I_h, we examined the impact of the selective HCN channel blocker zatebradine on hyperpolarization-induced inward currents in *mTOR*^{S2215Y} neurons to further confirm the identity of ΔI as I_h. Application of 40 µM zatebradine reduced the overall inward currents (**Fig. 3g, h, Table 1**) and ΔI (**Fig. 3i, Table 1**). At -90 mV, ΔI was significantly decreased from -167.7 ± 54.2 pA to 0.75 ± 8.2 pA (± SD) (**Fig. 3i,** arrow). Subtraction of the post- from the pre-zatebradine current traces isolated zatebradine-sensitive inward currents which reversed near -50 mV, as previously reported for HCN4 channel reversal potentials[33] (**Fig. 3j, k, Table 1)**. These experiments verified the identity of ΔI as I_h. In comparison, application of the Kir channel blocker barium chloride ($BaCl_2$) substantially reduced the overall inward currents but had no effects on ΔI (i.e., I_h) in *Tsc1*^{KO} neurons (**Fig. S6a-i**). Consistent with the function of I_h in maintaining RMP at depolarized levels[34-38], application of zatebradine

hyperpolarized RMP in *mTOR*^{S2215Y} neurons but did not affect the RMP of control neurons that exhibited no I_h (**Fig. 3l, Table 1**). Collectively, these findings suggest that *Rheb*^{Y35L}, *mTOR*^{S2215Y}, *Dedpdc5*^{KO}, *Pten*^{KO}, and *Tsc1*^{KO} expression in layer 2/3 pyramidal neurons lead to the abnormal presence of HCN4 channels with variations in functional expression.

Expression of *Rheb*^{Y35L}, *mTOR*^{S2215Y}, *Dedpdc5*^{KO}, *Pten*^{KO}, and *Tsc1*^{KO} leads to different impacts on excitatory synaptic activity

As part of examining neuron excitability, we recorded spontaneous excitatory postsynaptic currents (sEPSCs) in all the gene conditions. The frequency of sEPSCs was unchanged in all experimental conditions except for the *Tsc1*^{KO} condition, in which the frequency was significantly increased (**Fig. 4a, b, Table 1, Fig. S7a**). Unlike the other experimental conditions, the *Rheb*^{Y35L} condition displayed a slight decrease in sEPSC frequency, consistent with previous findings in *Rheb*^{S16H} neurons; however, this did not reach statistical significance (**Fig. 4b**). The amplitude of sEPSCs was larger in the *Rheb*^{Y35L}, *mTOR*^{S2215Y,} and *Pten*^{KO} conditions (**Fig. 4a, c, Table 1, Fig. S7b**). Although the amplitudes were slightly larger in the *Depdc5*^{KO} and *Tsc1*^{KO} conditions, these changes were not significant (**Fig. 4c**). Thus, *Tsc1*^{KO} neurons display increased sEPSC frequency but unchanged amplitude, while *Rheb*^{Y35L}, *mTOR*^{S2215Y,} and *Pten*^{KO} neurons display increased sEPSC amplitude but unchanged frequency. Finally, there was an increase in the sEPSC total charge in all experimental conditions except for the *Rheb*^{Y35L} condition (**Fig. 4d, Table 1, Fig. S7c)**. Collectively, these findings suggest all experimental conditions, except for *Rheb*^{Y35L}, lead to increased synaptic excitability, with variable impact on sEPSC frequency and amplitude.

DISCUSSION

In this unprecedented comparison study, we examined the impacts of several distinct epilepsy-associated mTORC1 pathway gene mutations on cortical pyramidal neuron development and their electrophysiological properties and synaptic integration in the mouse mPFC. Through a combination of IUE to model the genetic mosaicism of FMCDs, histological analyses, and patch-clamp electrophysiological recordings, we found that activation of either *Rheb* or *mTOR* or biallelic inactivation *Depdc5*, *Tsc1*, or *Pten*, all of which increase mTORC1 activity, largely leads to similar alterations in neuron morphology and membrane excitability but differentially impacts excitatory synaptic transmission. These findings have significant implications for understanding

the mechanisms leading to cortical hyperexcitability and seizures in mTORC1-driven FMCDs and highlight the utility of personalized medicine dictated by patient gene variants.

Several histological phenotypes associated with mTORC1 hyperactivation were anticipated and confirmed in our studies. We found increased neuron soma size across all gene conditions, consistent with previous reports[24,26,27,39-42]. Additionally, all conditions, except for *Pten*^{KO}, resulted in neuronal mispositioning in the mPFC, with *Rheb*^{Y35L} and *mTOR*^{S2215Y} conditions being the most severe. Interestingly, *Pten*^{KO} neurons were correctly placed in layer 2/3, despite having one of the largest soma size increases, suggesting that cell positioning is independent of cell size. The lack of mispositioning of *Pten*^{KO} neurons was surprising as it is thought that increased mTORC1 activity leads to neuronal misplacement, and aberrant migration of *Pten*^{KO} neurons has been reported in the hippocampus[43]. Given that PTEN has a long half-life, with a reported range of 5 to 20 hours or more depending on the cell type[44-51], it is possible that following knockout at E15, the decreases in existing protein levels lagged behind the time window to affect neuronal migration. However, TSC1 also has a long half-life of ~22 hours[52,53], and knockout of *Tsc1* at the same time point was sufficient to affect neuronal positioning. Mispositioning of neurons following *Pten* knockout in E15 rats was reported by one study, but this was a very mild phenotype compared to findings in the other gene conditions[39]. Therefore, these data suggest that PTEN has gene-specific biological mechanisms that contribute to the lack of severe neuronal mispositioning in the developing cortex. *mTOR*^{S2215Y} exhibited the strongest phenotypes in terms of neuron size and positioning, which is perhaps not surprising as the mTOR protein itself forms the catalytic subunit of mTORC1. *Depdc5*^{KO} exhibited the mildest changes in these parameters. Unlike PTEN, TSC1, RHEB, and mTOR, which regulate mTORC1 via the canonical PI3K-mTORC1 pathway in response to growth factor stimulation, DEPDC5 regulates mTORC1 via the GATOR1 complex in response to changes in cellular amino acid levels[54]. The different modes of mTORC1 regulation by DEPDC5 may contribute to the differences in the severity of the phenotypes.

To assess the impact of RHEB, mTOR, DEPDC5, PTEN, and TSC1 disruption on cortical neuron excitability, we examined the intrinsic biophysical and synaptic properties of layer 2/3 pyramidal neurons in the mPFC. We found that all gene manipulations led to increased membrane conductance but decreased AP firing upon membrane depolarization, consistent with previous reports in the somatosensory cortex[26,39,42,55-58] and in the mPFC for the *Rheb*^{S16H} condition[30,31]. Neurons in these conditions required a larger depolarization to generate an AP (increased

rheobase), likely due to their enlarged cell size. These findings seem to contradict the theory that seizure initiation originates from these neurons. However, inhibiting firing in cortical pyramidal neurons expressing the mTORC1-activating *Rheb*^{S16H} mutation via co-expression with Kir2.1 channels (to hyperpolarize neurons) has been shown to prevent seizures, supporting a cell-autonomous mechanism[30]. This discrepancy may be reconciled by the identification of abnormal HCN4 channel expression in the *Rheb*^{S16H} neurons, which was shown to contribute to increased excitability by depolarizing RMPs, bringing neurons closer to the AP threshold, and conferring firing sensitivity to cyclic AMP[30]. The abnormal HCN4 channel expression has been verified in resected human FCDII and HME tissue (of unknown genetic etiology)[30]. Here, we found that *Rheb*^{Y35L}, *mTOR*^{S2215Y}, *Depdc5*^{KO}, *Pten*^{KO}, and *Tsc1*^{KO} cortical neurons also display aberrant HCN4 channel expression, which is consistent with the rapamycin- and 4E-BP1-dependent mode of expression in *Rheb*^{S16H} neurons[30,31]. The functional expression of these channels was variable, and the corresponding changes in I_h did not reach statistical significance for *Rheb*^{Y35L}, *Depdc5*^{KO}, and *Pten*^{KO} neurons. Nonetheless, consistent with the function of HCN4 channels in maintaining the RMP at depolarized levels[38], *Rheb*^{Y35L}, *mTOR*^{S2215Y}, and *Tsc1*^{KO} neurons exhibited depolarized RMPs. Interestingly, the RMP was unchanged in *Pten*^{KO} and *Depdc5*^{KO} neurons. The lack of RMP changes may be explained by the milder HCN4 phenotype or the presence of different ion channel complements in these neurons. In addition to HCN4 channels, it is thought that increased Kir channels, which are well-known to hyperpolarize RMPs, contribute to the enlarged inward currents in all the conditions we investigated. This was confirmed in the *Tsc1*^{KO} neurons where application of $BaCl_2$ to block Kir channels reduced the overall inward current and depolarized RMPs. Since *Pten*^{KO} neurons have a larger overall inward current but a smaller I_h compared to *Tsc1*^{KO} neurons, we postulate that *Pten*^{KO} neurons have a higher expression of Kir channels neurons that could counteract the HCN4 channels' depolarizing effect on RMP. The mechanisms and functional significance of the Kir channel increases in these neurons are yet to be validated. Nevertheless, our data suggest that abnormal HCN4 channel expression is a conserved mechanism across these gene conditions and warrant further investigation of HCN-mediated excitability in mTORC1-related epilepsy.

While membrane excitability was largely similar across all gene conditions, the excitatory synaptic properties were more variable. All conditions, except for *Rheb*^{Y35L}, led to increased excitatory synaptic activity, with variable impact on sEPSC frequency and amplitude. *Tsc1*^{KO}

neurons were the only investigated condition that displayed increased sEPSC frequency. This finding corroborates a previous study showing increased sEPSC frequency with no sEPSC amplitude changes in layer 2/3 cortical pyramidal neurons from 4-week-old *Tsc1* conditional KO mice[58]. Interestingly, as previously reported for *Rheb*^{S16H} neurons[59], the sEPSC frequency in *Rheb*^{Y35L} neurons was reduced by 25% but this did not reach statistical significance, possibly due to a generally weaker effect of the Y35L mutation compared to the S16H mutation. *Rheb*^{Y35L}, *mTOR*^{S2215Y}, and *Pten*^{KO} neurons exhibited increased sEPSC amplitudes. We found no changes in the sEPSC amplitude of *Depdc5*^{KO} neurons, which differs from a previous study reporting increased sEPSC amplitude in these neurons[26]. This discrepancy may likely be explained by the differences in the age of the animals examined in their study (P20-24) versus ours (P26-43), given that dynamic changes in synaptic properties are still ongoing past P21[60]. Despite the above differences in sEPSC frequencies and amplitudes, the total charge was increased in almost all conditions except for in *Rheb*^{Y35L}, suggesting enhanced synaptic drive and connectivity. These excitatory synaptic changes may counteract the increases in rheobase (i.e., decreased membrane excitability) and thereby impact circuit hyperexcitability and seizure vulnerability. Overall, the changes in synaptic activity for the *Rheb*^{Y35L} condition are in stark contrast to the other gene conditions. These observations suggest a Rheb-specific impact on synaptic activity that differs from the other mTORC1 pathway genes. Thus, despite impinging on mTORC1 signaling, different mTORC1 pathway gene mutations can affect synaptic activity, and thereby, excitability differently. The mechanisms accounting for the observed differences are not clear, but it is increasingly acknowledged that additional pathways beyond mTORC1 are activated by each gene condition that could contribute to the differential impacts on synaptic activity[13]. One limitation of this study is that we did not examine inhibitory synaptic properties and the impact on excitatory-inhibitory balance. These changes could potentially contribute to gene-specific mechanisms of cortical hyperexcitability and should be the subject of another study.

In summary, we have shown that mutations affecting different mTORC1 pathway genes have similar and dissimilar consequences on cortical pyramidal neuron development and function, which may affect how neurons behave in cortical circuits. Our findings suggest that cortical neurons harboring different mTORC1 pathway gene mutations may differentially affect how neurons receive and process cortical inputs, which have implications for the mechanisms of

cortical hyperexcitability and seizures in FMCDs, and potentially affect how neurons and their networks respond to therapeutic intervention.

Author contribution: LN: conceptualization, investigation, analysis, visualization, writing-original draft, review & editing, YX: investigation, analysis, MN: analysis, AB: conceptualization, writing-original draft, review & editing.

Data availability: The datasets generated during and/or analyzed during the current study are available from the corresponding authors upon reasonable request.

Competing interest: AB is an inventor on a patent application "Methods of treating and diagnosing epilepsy" (Pub. no. US2022/0143219 A1).

Grant funding: National Institutes of Health (NIH) F32 HD095567 (LHN), R01 NS111980 (AB)

Acknowledgments: We thank Drs. Stéphanie Baulac (Paris Brain Institute, France) for providing the pX330-*Depdc5* plasmid and Dr. Joseph LoTurco (University of Connecticut) for insightful discussions and advice on the pX330-*Tsc1* plasmid.

References

1 Harvey, A. S., Cross, J. H., Shinnar, S., Mathern, G. W. & Taskforce, I. P. E. S. S. Defining the spectrum of international practice in pediatric epilepsy surgery patients. *Epilepsia* **49**, 146-155 (2008). https://doi.org:10.1111/j.1528-1167.2007.01421.x

2 Blumcke, I., Spreafico, R., Haaker, G., Coras, R., Kobow, K., Bien, C. G., Pfafflin, M., Elger, C., Widman, G., Schramm, J., Becker, A., Braun, K. P., Leijten, F., Baayen, J. C., Aronica, E., Chassoux, F., Hamer, H., Stefan, H., Rossler, K., Thom, M., . . . Consortium, E. Histopathological Findings in Brain Tissue Obtained during Epilepsy Surgery. *N Engl J Med* **377**, 1648-1656 (2017). https://doi.org:10.1056/NEJMoa1703784

3 Guerrini, R. & Dobyns, W. B. Malformations of cortical development: clinical features and genetic causes. *Lancet Neurol* **13**, 710-726 (2014). https://doi.org:10.1016/S1474-4422(14)70040-7

4 Crino, P. B. Focal brain malformations: seizures, signaling, sequencing. *Epilepsia* **50 Suppl 9**, 3-8 (2009). https://doi.org:10.1111/j.1528-1167.2009.02289.x

5 Marsan, E. & Baulac, S. Review: Mechanistic target of rapamycin (mTOR) pathway, focal cortical dysplasia and epilepsy. *Neuropathol Appl Neurobiol* **44**, 6-17 (2018). https://doi.org:10.1111/nan.12463

6 Muhlebner, A., Bongaarts, A., Sarnat, H. B., Scholl, T. & Aronica, E. New insights into a spectrum of developmental malformations related to mTOR dysregulations: challenges and perspectives. *J Anat* **235**, 521-542 (2019). https://doi.org:10.1111/joa.12956

7 Gerasimenko, A., Baldassari, S. & Baulac, S. mTOR pathway: Insights into an established pathway for brain mosaicism in epilepsy. *Neurobiol Dis* **182**, 106144 (2023). https://doi.org:10.1016/j.nbd.2023.106144

8 D'Gama, A. M., Woodworth, M. B., Hossain, A. A., Bizzotto, S., Hatem, N. E., LaCoursiere, C. M., Najm, I., Ying, Z., Yang, E., Barkovich, A. J., Kwiatkowski, D. J., Vinters, H. V., Madsen, J. R., Mathern, G. W., Blumcke, I., Poduri, A. & Walsh, C. A. Somatic Mutations Activating the mTOR Pathway in Dorsal Telencephalic Progenitors Cause a Continuum of Cortical Dysplasias. *Cell Rep* **21**, 3754-3766 (2017). https://doi.org:10.1016/j.celrep.2017.11.106

9 Chung, C., Yang, X., Bae, T., Vong, K. I., Mittal, S., Donkels, C., Westley Phillips, H., Li, Z., Marsh, A. P. L., Breuss, M. W., Ball, L. L., Garcia, C. A. B., George, R. D., Gu, J., Xu, M., Barrows, C., James, K. N., Stanley, V., Nidhiry, A. S., Khoury, S., . . . Gleeson, J. G. Comprehensive multi-omic profiling of somatic mutations in malformations of cortical development. *Nat Genet* **55**, 209-220 (2023). https://doi.org:10.1038/s41588-022-01276-9

10 Laplante, M. & Sabatini, D. M. mTOR signaling in growth control and disease. *Cell* **149**, 274-293 (2012). https://doi.org:10.1016/j.cell.2012.03.017

11 Dibble, C. C. & Cantley, L. C. Regulation of mTORC1 by PI3K signaling. *Trends Cell Biol* **25**, 545-555 (2015). https://doi.org:10.1016/j.tcb.2015.06.002

12 Bar-Peled, L. & Sabatini, D. M. Regulation of mTORC1 by amino acids. *Trends Cell Biol* **24**, 400-406 (2014). https://doi.org:10.1016/j.tcb.2014.03.003

13 Nguyen, L. H. & Bordey, A. Convergent and Divergent Mechanisms of Epileptogenesis in mTORopathies. *Front Neuroanat* **15**, 664695 (2021). https://doi.org:10.3389/fnana.2021.664695

14 Nguyen, L. H. & Bordey, A. Current Review in Basic Science: Animal Models of Focal Cortical Dysplasia and Epilepsy. *Epilepsy Curr* **22**, 234-240 (2022). https://doi.org:10.1177/15357597221098230

15 Neuman, N. A. & Henske, E. P. Non-canonical functions of the tuberous sclerosis complex-Rheb signalling axis. *EMBO Mol Med* **3**, 189-200 (2011). https://doi.org:10.1002/emmm.201100131

16 Chetram, M. A. & Hinton, C. V. PTEN regulation of ERK1/2 signaling in cancer. *J Recept Signal Transduct Res* **32**, 190-195 (2012). https://doi.org:10.3109/10799893.2012.695798

17 Lien, E. C., Dibble, C. C. & Toker, A. PI3K signaling in cancer: beyond AKT. *Curr Opin Cell Biol* **45**, 62-71 (2017). https://doi.org:10.1016/j.ceb.2017.02.007

18 Manning, B. D. & Toker, A. AKT/PKB Signaling: Navigating the Network. *Cell* **169**, 381-405 (2017). https://doi.org:10.1016/j.cell.2017.04.001

19 Swaminathan, A., Hassan-Abdi, R., Renault, S., Siekierska, A., Riche, R., Liao, M., de Witte, P. A. M., Yanicostas, C., Soussi-Yanicostas, N., Drapeau, P. & Samarut, E. Non-canonical mTOR-Independent Role of DEPDC5 in Regulating GABAergic Network Development. *Curr Biol* **28**, 1924-1937 e1925 (2018). https://doi.org:10.1016/j.cub.2018.04.061

20 Nakashima, M., Saitsu, H., Takei, N., Tohyama, J., Kato, M., Kitaura, H., Shiina, M., Shirozu, H., Masuda, H., Watanabe, K., Ohba, C., Tsurusaki, Y., Miyake, N., Zheng, Y., Sato, T., Takebayashi, H., Ogata, K., Kameyama, S., Kakita, A. & Matsumoto, N. Somatic Mutations in the MTOR gene cause focal cortical dysplasia type IIb. *Ann Neurol* **78**, 375-386 (2015). https://doi.org:10.1002/ana.24444

21 Mirzaa, G. M., Campbell, C. D., Solovieff, N., Goold, C., Jansen, L. A., Menon, S., Timms, A. E., Conti, V., Biag, J. D., Adams, C., Boyle, E. A., Collins, S., Ishak, G.,

Poliachik, S., Girisha, K. M., Yeung, K. S., Chung, B. H. Y., Rahikkala, E., Gunter, S. A., McDaniel, S. S., . . . Dobyns, W. B. Association of MTOR Mutations With Developmental Brain Disorders, Including Megalencephaly, Focal Cortical Dysplasia, and Pigmentary Mosaicism. *JAMA Neurol* **73**, 836-845 (2016). https://doi.org:10.1001/jamaneurol.2016.0363

22 Moller, R. S., Weckhuysen, S., Chipaux, M., Marsan, E., Taly, V., Bebin, E. M., Hiatt, S. M., Prokop, J. W., Bowling, K. M., Mei, D., Conti, V., de la Grange, P., Ferrand-Sorbets, S., Dorfmuller, G., Lambrecq, V., Larsen, L. H., Leguern, E., Guerrini, R., Rubboli, G., Cooper, G. M., . . . Baulac, S. Germline and somatic mutations in the MTOR gene in focal cortical dysplasia and epilepsy. *Neurol Genet* **2**, e118 (2016). https://doi.org:10.1212/NXG.0000000000000118

23 Baldassari, S., Ribierre, T., Marsan, E., Adle-Biassette, H., Ferrand-Sorbets, S., Bulteau, C., Dorison, N., Fohlen, M., Polivka, M., Weckhuysen, S., Dorfmuller, G., Chipaux, M. & Baulac, S. Dissecting the genetic basis of focal cortical dysplasia: a large cohort study. *Acta Neuropathol* **138**, 885-900 (2019). https://doi.org:10.1007/s00401-019-02061-5

24 Zhao, S., Li, Z., Zhang, M., Zhang, L., Zheng, H., Ning, J., Wang, Y., Wang, F., Zhang, X., Gan, H., Wang, Y., Zhang, X., Luo, H., Bu, G., Xu, H., Yao, Y. & Zhang, Y. W. A brain somatic RHEB doublet mutation causes focal cortical dysplasia type II. *Exp Mol Med* **51**, 1-11 (2019). https://doi.org:10.1038/s12276-019-0277-4

25 Lee, W. S., Baldassari, S., Chipaux, M., Adle-Biassette, H., Stephenson, S. E. M., Maixner, W., Harvey, A. S., Lockhart, P. J., Baulac, S. & Leventer, R. J. Gradient of brain mosaic RHEB variants causes a continuum of cortical dysplasia. *Ann Clin Transl Neurol* **8**, 485-490 (2021). https://doi.org:10.1002/acn3.51286

26 Ribierre, T., Deleuze, C., Bacq, A., Baldassari, S., Marsan, E., Chipaux, M., Muraca, G., Roussel, D., Navarro, V., Leguern, E., Miles, R. & Baulac, S. Second-hit mosaic mutation in mTORC1 repressor DEPDC5 causes focal cortical dysplasia-associated epilepsy. *J Clin Invest* **128**, 2452-2458 (2018). https://doi.org:10.1172/JCI99384

27 Lim, J. S., Gopalappa, R., Kim, S. H., Ramakrishna, S., Lee, M., Kim, W. I., Kim, J., Park, S. M., Lee, J., Oh, J. H., Kim, H. D., Park, C. H., Lee, J. S., Kim, S., Kim, D. S., Han, J. M., Kang, H. C., Kim, H. H. & Lee, J. H. Somatic Mutations in TSC1 and TSC2 Cause Focal Cortical Dysplasia. *Am J Hum Genet* **100**, 454-472 (2017). https://doi.org:10.1016/j.ajhg.2017.01.030

28 Xue, W., Chen, S., Yin, H., Tammela, T., Papagiannakopoulos, T., Joshi, N. S., Cai, W., Yang, G., Bronson, R., Crowley, D. G., Zhang, F., Anderson, D. G., Sharp, P. A. & Jacks, T. CRISPR-mediated direct mutation of cancer genes in the mouse liver. *Nature* **514**, 380-384 (2014). https://doi.org:10.1038/nature13589

29 Kroon, T., van Hugte, E., van Linge, L., Mansvelder, H. D. & Meredith, R. M. Early postnatal development of pyramidal neurons across layers of the mouse medial prefrontal cortex. *Sci Rep* **9**, 5037 (2019). https://doi.org:10.1038/s41598-019-41661-9

30 Hsieh, L. S., Wen, J. H., Nguyen, L. H., Zhang, L., Getz, S. A., Torres-Reveron, J., Wang, Y., Spencer, D. D. & Bordey, A. Ectopic HCN4 expression drives mTOR-dependent epilepsy in mice. *Sci Transl Med* **12** (2020). https://doi.org:10.1126/scitranslmed.abc1492

31 Nguyen, L. H., Xu, Y., Mahadeo, T., Zhang, L., Lin, T. V., Born, H. A., Anderson, A. E. & Bordey, A. Expression of 4E-BP1 in juvenile mice alleviates mTOR-induced neuronal

dysfunction and epilepsy. *Brain* **145**, 1310-1325 (2022). https://doi.org:10.1093/brain/awab390

32 Thoby-Brisson, M., Telgkamp, P. & Ramirez, J. M. The role of the hyperpolarization-activated current in modulating rhythmic activity in the isolated respiratory network of mice. *J Neurosci* **20**, 2994-3005 (2000).

33 Tae, H. S., Smith, K. M., Phillips, A. M., Boyle, K. A., Li, M., Forster, I. C., Hatch, R. J., Richardson, R., Hughes, D. I., Graham, B. A., Petrou, S. & Reid, C. A. Gabapentin Modulates HCN4 Channel Voltage-Dependence. *Front Pharmacol* **8**, 554 (2017). https://doi.org:10.3389/fphar.2017.00554

34 Lamas, J. A. A hyperpolarization-activated cation current (Ih) contributes to resting membrane potential in rat superior cervical sympathetic neurones. *Pflugers Arch* **436**, 429-435 (1998). https://doi.org:10.1007/s004240050653

35 Doan, T. N. & Kunze, D. L. Contribution of the hyperpolarization-activated current to the resting membrane potential of rat nodose sensory neurons. *J Physiol* **514 (Pt 1)**, 125-138 (1999). https://doi.org:10.1111/j.1469-7793.1999.125af.x

36 Lupica, C. R., Bell, J. A., Hoffman, A. F. & Watson, P. L. Contribution of the hyperpolarization-activated current (I(h)) to membrane potential and GABA release in hippocampal interneurons. *J Neurophysiol* **86**, 261-268 (2001). https://doi.org:10.1152/jn.2001.86.1.261

37 Funahashi, M., Mitoh, Y., Kohjitani, A. & Matsuo, R. Role of the hyperpolarization-activated cation current (Ih) in pacemaker activity in area postrema neurons of rat brain slices. *J Physiol* **552**, 135-148 (2003). https://doi.org:10.1113/jphysiol.2003.047191

38 Kase, D. & Imoto, K. The Role of HCN Channels on Membrane Excitability in the Nervous System. *J Signal Transduct* **2012**, 619747 (2012). https://doi.org:10.1155/2012/619747

39 Chen, F., Rosiene, J., Che, A., Becker, A. & LoTurco, J. Tracking and transforming neocortical progenitors by CRISPR/Cas9 gene targeting and piggyBac transposase lineage labeling. *Development* **142**, 3601-3611 (2015). https://doi.org:10.1242/dev.118836

40 Lim, J. S., Kim, W. I., Kang, H. C., Kim, S. H., Park, A. H., Park, E. K., Cho, Y. W., Kim, S., Kim, H. M., Kim, J. A., Kim, J., Rhee, H., Kang, S. G., Kim, H. D., Kim, D., Kim, D. S. & Lee, J. H. Brain somatic mutations in MTOR cause focal cortical dysplasia type II leading to intractable epilepsy. *Nat Med* **21**, 395-400 (2015). https://doi.org:10.1038/nm.3824

41 Hsieh, L. S., Wen, J. H., Claycomb, K., Huang, Y. G., Harrsch, F. A., Naegele, J. R., Hyder, F., Buchanan, G. F. & Bordey, A. Convulsive seizures from experimental focal cortical dysplasia occur independently of cell misplacement. *Nat Commun* **7** (2016). https://doi.org:ARTN 11753
10.1038/ncomms11753

42 Proietti Onori, M., Koene, L. M. C., Schafer, C. B., Nellist, M., de Brito van Velze, M., Gao, Z., Elgersma, Y. & van Woerden, G. M. RHEB/mTOR hyperactivity causes cortical malformations and epileptic seizures through increased axonal connectivity. *PLoS Biol* **19**, e3001279 (2021). https://doi.org:10.1371/journal.pbio.3001279

43 Getz, S. A., DeSpenza, T., Jr., Li, M. & Luikart, B. W. Rapamycin prevents, but does not reverse, aberrant migration in Pten knockout neurons. *Neurobiol Dis* **93**, 12-20 (2016). https://doi.org:10.1016/j.nbd.2016.03.010

44 Trotman, L. C., Wang, X., Alimonti, A., Chen, Z., Teruya-Feldstein, J., Yang, H., Pavletich, N. P., Carver, B. S., Cordon-Cardo, C., Erdjument-Bromage, H., Tempst, P., Chi, S. G., Kim, H. J., Misteli, T., Jiang, X. & Pandolfi, P. P. Ubiquitination regulates PTEN nuclear import and tumor suppression. *Cell* **128**, 141-156 (2007). https://doi.org:10.1016/j.cell.2006.11.040

45 Mukherjee, R., Vanaja, K. G., Boyer, J. A., Gadal, S., Solomon, H., Chandarlapaty, S., Levchenko, A. & Rosen, N. Regulation of PTEN translation by PI3K signaling maintains pathway homeostasis. *Mol Cell* **81**, 708-723 e705 (2021). https://doi.org:10.1016/j.molcel.2021.01.033

46 Li, H., Zhang, P., Zhang, Q., Li, C., Zou, W., Chang, Z., Cui, C. P. & Zhang, L. WWP2 is a physiological ubiquitin ligase for phosphatase and tensin homolog (PTEN) in mice. *J Biol Chem* **293**, 8886-8899 (2018). https://doi.org:10.1074/jbc.RA117.001060

47 Wong, C. W., Or, P. M. Y., Wang, Y., Li, L., Li, J., Yan, M., Cao, Y., Luk, H. M., Tong, T. M. F., Leslie, N. R., Lo, I. F., Choy, K. W. & Chan, A. M. L. Identification of a PTEN mutation with reduced protein stability, phosphatase activity, and nuclear localization in Hong Kong patients with autistic features, neurodevelopmental delays, and macrocephaly. *Autism Res* **11**, 1098-1109 (2018). https://doi.org:10.1002/aur.1950

48 Yang, Y., Zhou, F., Fang, Z., Wang, L., Li, Z., Sun, L., Wang, C., Yao, W., Cai, X., Jin, J. & Zha, X. Post-transcriptional and post-translational regulation of PTEN by transforming growth factor-beta1. *J Cell Biochem* **106**, 1102-1112 (2009). https://doi.org:10.1002/jcb.22100

49 Yim, E. K., Peng, G., Dai, H., Hu, R., Li, K., Lu, Y., Mills, G. B., Meric-Bernstam, F., Hennessy, B. T., Craven, R. J. & Lin, S. Y. Rak functions as a tumor suppressor by regulating PTEN protein stability and function. *Cancer Cell* **15**, 304-314 (2009). https://doi.org:10.1016/j.ccr.2009.02.012

50 Vazquez, F., Ramaswamy, S., Nakamura, N. & Sellers, W. R. Phosphorylation of the PTEN tail regulates protein stability and function. *Mol Cell Biol* **20**, 5010-5018 (2000). https://doi.org:10.1128/MCB.20.14.5010-5018.2000

51 Sacco, J. J., Yau, T. Y., Darling, S., Patel, V., Liu, H., Urbe, S., Clague, M. J. & Coulson, J. M. The deubiquitylase Ataxin-3 restricts PTEN transcription in lung cancer cells. *Oncogene* **33**, 4265-4272 (2014). https://doi.org:10.1038/onc.2013.512

52 Lee, D. F., Kuo, H. P., Chen, C. T., Wei, Y., Chou, C. K., Hung, J. Y., Yen, C. J. & Hung, M. C. IKKbeta suppression of TSC1 function links the mTOR pathway with insulin resistance. *Int J Mol Med* **22**, 633-638 (2008). https://doi.org:10.3892/ijmm_00000065

53 Alquezar, C., Schoch, K. M., Geier, E. G., Ramos, E. M., Scrivo, A., Li, K. H., Argouarch, A. R., Mlynarski, E. E., Dombroski, B., DeTure, M., Dickson, D. W., Yokoyama, J. S., Cuervo, A. M., Burlingame, A. L., Schellenberg, G. D., Miller, T. M., Miller, B. L. & Kao, A. W. TSC1 loss increases risk for tauopathy by inducing tau acetylation and preventing tau clearance via chaperone-mediated autophagy. *Sci Adv* **7**, eabg3897 (2021). https://doi.org:10.1126/sciadv.abg3897

54 Iffland, P. H., 2nd, Carson, V., Bordey, A. & Crino, P. B. GATORopathies: The role of amino acid regulatory gene mutations in epilepsy and cortical malformations. *Epilepsia* **60**, 2163-2173 (2019). https://doi.org:10.1111/epi.16370

55 Hu, S., Knowlton, R. C., Watson, B. O., Glanowska, K. M., Murphy, G. G., Parent, J. M. & Wang, Y. Somatic Depdc5 deletion recapitulates electroclinical features of human

focal cortical dysplasia type IIA. *Ann Neurol* **84**, 140-146 (2018). https://doi.org:10.1002/ana.25272

56 Goz, R. U., Akgul, G. & LoTurco, J. J. BRAFV600E expression in neural progenitors results in a hyperexcitable phenotype in neocortical pyramidal neurons. *J Neurophysiol* **123**, 2449-2464 (2020). https://doi.org:10.1152/jn.00523.2019

57 Koh, H. Y., Jang, J., Ju, S. H., Kim, R., Cho, G. B., Kim, D. S., Sohn, J. W., Paik, S. B. & Lee, J. H. Non-Cell Autonomous Epileptogenesis in Focal Cortical Dysplasia. *Ann Neurol* **90**, 285-299 (2021). https://doi.org:10.1002/ana.26149

58 Wu, X., Sosunov, A. A., Lado, W., Teoh, J. J., Ham, A., Li, H., Al-Dalahmah, O., Gill, B. J. A., Arancio, O., Schevon, C. A., Frankel, W. N., McKhann, G. M., 2nd, Sulzer, D., Goldman, J. E. & Tang, G. Synaptic hyperexcitability of cytomegalic pyramidal neurons contributes to epileptogenesis in tuberous sclerosis complex. *Cell Rep* **40**, 111085 (2022). https://doi.org:10.1016/j.celrep.2022.111085

59 Lin, T. V., Hsieh, L., Kimura, T., Malone, T. J. & Bordey, A. Normalizing translation through 4E-BP prevents mTOR-driven cortical mislamination and ameliorates aberrant neuron integration. *P Natl Acad Sci USA* **113**, 11330-11335 (2016). https://doi.org:10.1073/pnas.1605740113

60 Lohmann, C. & Kessels, H. W. The developmental stages of synaptic plasticity. *J Physiol* **592**, 13-31 (2014). https://doi.org:10.1113/jphysiol.2012.235119

61 Nguyen, L. H., Mahadeo, T. & Bordey, A. mTOR Hyperactivity Levels Influence the Severity of Epilepsy and Associated Neuropathology in an Experimental Model of Tuberous Sclerosis Complex and Focal Cortical Dysplasia. *J Neurosci* **39**, 2762-2773 (2019). https://doi.org:10.1523/Jneurosci.2260-18.2019

62 Moen, E. L., Fricano-Kugler, C. J., Luikart, B. W. & O'Malley, A. J. Analyzing Clustered Data: Why and How to Account for Multiple Observations Nested within a Study Participant? *PLoS One* **11**, e0146721 (2016). https://doi.org:10.1371/journal.pone.0146721

63 Yu, Z., Guindani, M., Grieco, S. F., Chen, L., Holmes, T. C. & Xu, X. Beyond t test and ANOVA: applications of mixed-effects models for more rigorous statistical analysis in neuroscience research. *Neuron* **110**, 21-35 (2022). https://doi.org:10.1016/j.neuron.2021.10.030

64 Breunig, J. J., Gate, D., Levy, R., Rodriguez, J., Kim, G. B., Danielpour, M., Svendsen, C. N. & Town, T. Rapid genetic targeting of pial surface neural progenitors and immature neurons by neonatal electroporation. *Neural Dev* **7** (2012). https://doi.org:Artn 26 10.1186/1749-8104-7-26

METHODS

Animals

All animal procedures were performed in accordance with Yale University Institutional Animal Care and Use Committee's regulations. All experiments were performed on male and female CD-1 mice (Charles River Laboratories).

Plasmid DNA

Information on the plasmids used in this study is listed in **Table 2.** Concentrations of plasmids used for each control and experimental condition are listed in **Table 3**.

In utero electroporation (IUE)

Timed-pregnant embryonic day (E) 15.5 mice were anesthetized with isoflurane, and a midline laparotomy was performed to expose the uterine horns. A DNA plasmid solution was injected into the right lateral ventricle of each embryo using a glass pipette. For each litter, half of the embryos received plasmids for the experimental condition and the other half received plasmids for the respective control condition. A 5 mm tweezer electrode was positioned on the embryo head and 6 x 42V, 50 ms pulses at 950 ms intervals were applied using a pulse generator (ECM830, BTX) to electroporate the plasmids into neural progenitor cells. Electrodes were positioned to target expression in the mPFC. The embryos were returned to the abdominal cavity and allowed to continue with development. At P0, mice were screened under a fluorescence stereomicroscope to ensure electroporation success, as defined by fluorescence in the targeted brain region, before proceeding with downstream experiments

Brain fixation and immunofluorescent staining

P7-9 (neonates) and P28-43 (young adults) mice were deeply anesthetized with isoflurane and sodium pentobarbital (85 mg/kg i.p. injection) and perfused with ice-cold phosphate buffered saline (PBS) followed by ice-cold 4% PFA. Whole brains were dissected and post-fixed in 4% PFA for 2 hours and then cryoprotected in 30% sucrose for 24-48 hours at 4°C until they sank to the bottom of the tubes. Brains were serially cut into 50 µm-thick coronal sections using a freezing microtome and stored in PBS + 0.05% sodium azide at 4°C until use.

For immunofluorescence staining, free-floating brain sections were washed in PBS + 0.1% triton X-100 (PBS-T) for 2x10 min and permeabilized in PBS + 0.3% triton X-100 for 20-30 min. Sections were then incubated in blocking buffer (10% normal goat serum + 0.3% BSA + 0.3% triton X-100 in PBS) for 1 hour at room temperature and in primary antibodies **[**anti-p-S6 S240/244 (Cell Signaling Technology #5364, 1:1000) or anti-HCN4 (Alomone Labs APC-052, 1:500), diluted in 5% normal goat serum + 0.3% BSA + 0.1% triton X-100 in PBS**]** for 2 days at 4°C. Sections were then washed in PBS-T for 3x10 min, incubated in secondary antibodies **[**goat anti-rabbit IgG Alexa Fluor Plus 647 (Invitrogen #A32733, 1:500)**]** for 2 hours at room temperature, and again washed in PBS-T for 3x10 min. All sections were mounted onto microscope glass slides and coverslipped with ProLong Diamond Antifade Mountant (Invitrogen) for imaging. The specificity of the HCN4 antibodies was previously validated in our lab[30]. Additionally, a no primary antibody control was included to confirm the specificity of the secondary antibodies (**Fig. S5b**).

Confocal microscopy and image analysis

Images were acquired using a Zeiss LSM 880 confocal microscope. All image analyses were done using ImageJ software (NIH) and were performed blinded to experimental groups. Data were quantified using grayscale images of single optical sections. Representative images were prepared using Adobe Photoshop CC. All quantified images meant for direct comparison were taken with the same settings and uniformly processed.

P28-43 neuron soma size and p-S6 staining intensity were quantified from 20x magnification images of p-S6 stained brain sections by tracing the soma of randomly selected tdTomato+ cells and measuring the area and p-S6 intensity (mean gray value) within the same cell, respectively. HCN4 staining intensity was quantified from 20x magnification images by tracing the soma of randomly selected tdTomato+ cells and measuring HCN4 intensity (mean gray value). Staining intensities were normalized to the mean control. 15 cells from 2 brain sections per animal were analyzed for each of the parameters. Neuron positioning (% cells in layer 2/3) was quantified by counting the number of tdTomato+ cells within an 800 μm x 800 μm region of interest (ROI) on the electroporated cortex. Cells within 300 μm from the pial surface were considered correctly located in layer 2/3 whereas cells outside that boundary were considered misplaced[31,41,61]. The distribution of neurons in the cortex was further quantified by dividing the 800 μm x 800 μm ROI into 10 evenly spaced bins (bin width = 80 μm) parallel to the pial surface and counting the number of tdTomato+ cells in each bin. Only cells within the gray matter of the cortex were quantified. Data are shown as % of total tdTomato+ cell count. One brain section per animal was analyzed. P7-9 neuron soma size (supplemental data) was quantified from 10x magnification images of unstained brain sections by tracing the soma of randomly selected tdTomato+ cells and measuring the area. 30 cells from 2 sections per animal were analyzed.

Acute brain slice preparation, patch clamp recording, and analysis

P26-P51 mice were deeply anesthetized by carbon dioxide inhalation and sacrificed by decapitation. Whole brains were rapidly removed and immersed in ice-cold oxygenated (95% O_2/5%CO_2) high-sucrose cutting solution (in mM: 213 sucrose, 2.6 KCl, 1.25 NaH_2PO_4, 3 $MgSO_4$, 26 $NaHCO_3$, 10 Dextrose, 1 $CaCl_2$, 0.4 ascorbate, 4 Na-Lactate, 2 Na-Pyruvate, pH 7.4 with NaOH). 300 μm-thick coronal brain slices containing the mPFC were cut using a vibratome (Leica VT1000) and allowed to recover in a holding chamber with oxygenated artificial cerebrospinal fluid (aCSF, in mM: 118 NaCl, 3 KCl, 1.25 NaH_2PO_4, 1 $MgSO_4$, 26 $NaHCO_3$, 10 Dextrose, 2 $CaCl_2$, 0.4 ascorbate, 4 Na-Lactate, 2 Na-Pyruvate, 300 mOsm/kg, pH 7.4 with NaOH) for 30 min at 32°C before returning to room temperature (22°C) where they were kept for 6-8 hours during the experiment.

Whole-cell current- and voltage-clamp recordings were performed in a recording chamber at room temperature using pulled borosilicate glass pipettes (4-7 MΩ resistance, Sutter Instrument) filled with internal solution (in mM: 125 K-gluconate, 4 KCl, 10 HEPES, 1 EGTA, 0.2 $CaCl_2$, 10 di-tris-phosphocreatine, 4 Mg-ATP, 0.3 Na-GTP, 280 mOsm/kg, pH 7.3 with KOH). Fluorescent (i.e., electroporated) neurons in the mPFC were visualized using epifluorescence on an Olympus BX51WI microscope with a 40X water immersion objective. Recordings were performed on neurons in layer 2/3. Data were acquired using Axopatch 200B amplifier and pClamp 10 software (Molecular Devices) and filtered (at 5 kHz) and digitized using Digidata 1320 (Molecular Devices). All data analysis was performed offline using pClamp 10 software (Clampfit) and exported to GraphPad Prism 9 software for graphing and statistical analysis.

The RMP was recorded within the first 10 s after achieving whole-cell configuration at 0 pA in current-clamp mode. The membrane capacitance was measured in voltage-clamp mode and calculated by dividing the average membrane time constant by the average input resistance obtained from the current response to a 500-ms long (±5 mV) voltage step from -70 mV holding potential. The membrane time constant was determined from the biexponential curve best fitting the decay phase of the current; the slower component of the biexponential fit was used for the membrane time constant. The resting membrane conductance was measured in current-clamp mode and calculated using the membrane potential change induced by -500 pA hyperpolarizing current injections from rest. The AP input-output curve was generated by injecting 500 ms-long depolarizing currents steps from 0 to 400 pA in 20 pA increments from the RMP of each condition in current-clamp mode. The number of elicited APs was counted using the threshold search algorithm in Clampfit (pClamp). To determine the minimum amount of current needed to induce the first AP, i.e, rheobase, 5 ms-long depolarizing current steps in increments of 20 pA were applied every 3 s until an AP was elicited. The AP threshold, peak amplitude, and half-widths were analyzed from averaged traces of 5-10 consecutive APs induced by the rheobase +10 pA. The AP threshold was defined as the membrane potential at which the first derivative of an evoked AP achieved 10% of its peak velocity (dV/dt). The AP peak amplitude was defined as the difference between the peak and baseline. The AP half-width was defined as the duration of the AP at the voltage halfway between the peak and baseline. I_h was evoked by a series of 3 s-long hyperpolarizing voltage steps from -120 mV to -40 mV in 10 mV increments., with a holding potential of -70 mV. The I_h amplitudes (ΔI) were measured as the difference between the instantaneous current immediately following each test potential (I_{inst}) and the steady-state current at the end of each test potential (I_{ss})[32].

Zatebradine (40 µM, Toris Bioscience) and $BaCl_2$ (200 µM, Sigma-Aldrich) were applied locally to the recorded neurons via a large-tip (350 µM diameter) flow pipe. When no drugs were applied, a continuous flow of aCSF was supplied from the flow pipe. The IV curve, ΔIV curve, and RMP were measured before and after drug application as described above. The zatebradine-sensitive and $BaCl_2$ -sensitive currents were obtained by subtracting the current traces obtained after from before drug application. The IV curve for the zatebradine-sensitive current was obtained by measuring the steady-state of the resulting current, and the IV curve for the $BaCl_2$ -sensitive current was obtained by measuring the peak of the resulting current.

sEPSCs were recorded at a holding potential of -70 mV. Synaptic currents were recorded for a period of 2–5 min and analyzed by using the template search algorithm in Clampfit. The template was constructed by averaging 5-10 synaptic events, and the template match threshold parameter was adjusted to minimize false positives. All synaptic events identified by the program were manually inspected and non-synaptic currents (based on the fast-rising time) were discarded. The total charge (pA/ms) was calculated as area of sEPSC events (pA/ms) x frequency (Hz)/1000 for each neuron.

Statistical analysis

All statistical analyses were performed using GraphPad Prism 9 software with the significance level set at $p < 0.05$. Data were analyzed using nested t-test or nested one-way ANOVA (obtained by fitting a mixed-effects model wherein the main factor is treated as a fixed factor and the nested factor is treated as a random factor; to account for correlated data within individual animals within

groups[62,63]), one-way ANOVA, two-way repeated measure ANOVA, or mixed-effects ANOVA (fitted to a mixed-effects model for when values were missing values in repeated measures analyses), as appropriate. For all nested statistics, the distribution of data among individual animals is shown in **Supplemental Figs. S1, S3, S4,** and **S7**. All post-hoc analyses were performed using Holm-Šídák's multiple comparison test. The specific tests applied for each dataset, test results, and sample size (n, number of animals or neurons) are summarized in **Tables 1** and **S1** and described in the figure legends. All data are reported as the mean of all neurons or brain sections in each group ± standard error of the mean (SEM).

MAIN FIGURES AND TABLES

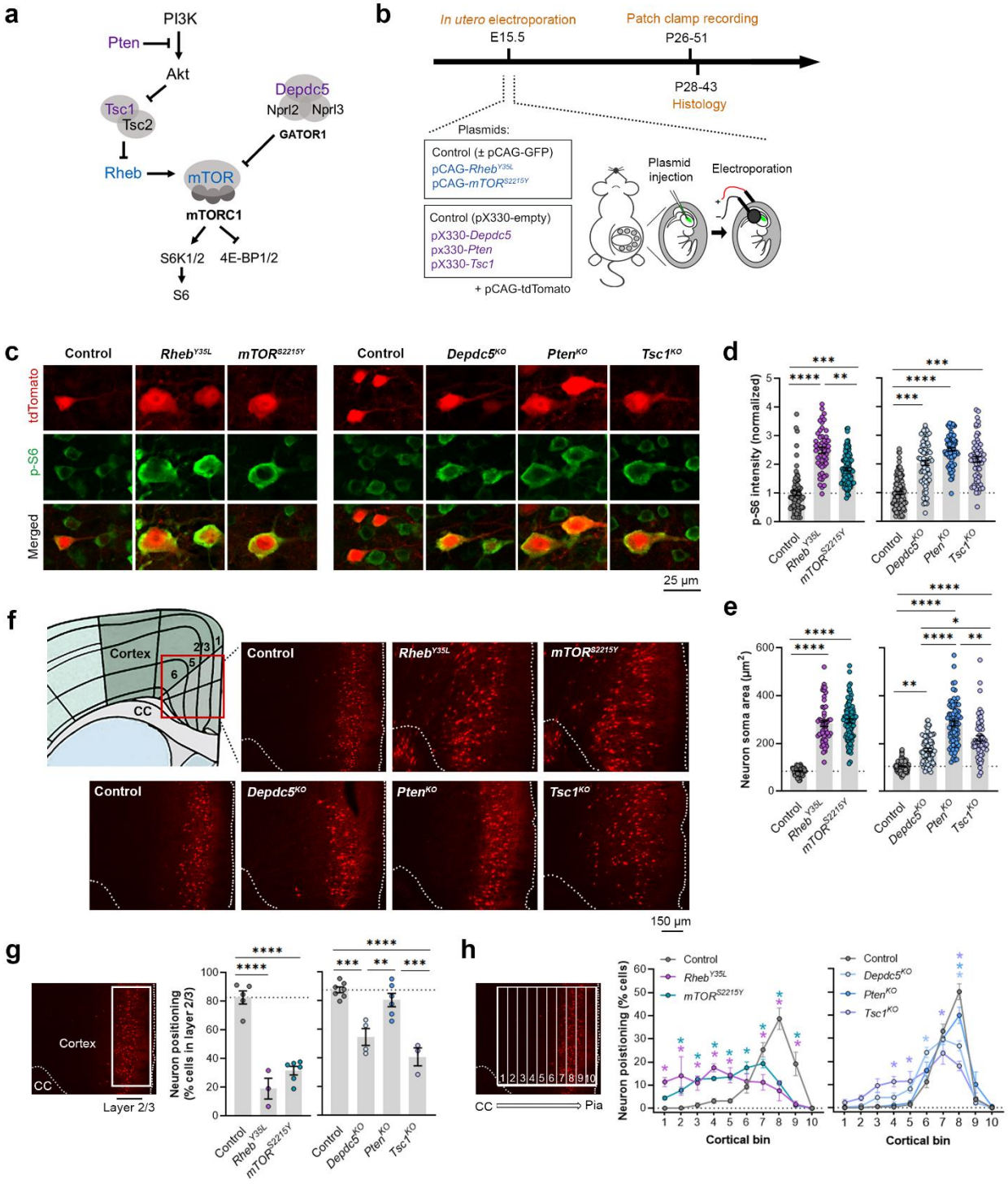

Figure 1: Expression of *Rheb*^{Y35L}, *mTOR*^{S2215Y}, *Dedpdc5*^{KO}, *Pten*^{KO}, and *Tsc1*^{KO} leads to varying magnitudes of neuronal enlargement and mispositioning in the cortex. (a) Diagram of the PI3K-mTORC1 pathway. Activation of mTORC1 signaling is controlled by positive (blue) and negative (purple) regulators within the pathway. **(b)** Diagram of overall experimental timeline and approach. IUE was performed at E15.5. A cohort of animals was used for patch clamp recording at P26-51 and another cohort was used for histology at P28-43. **(c)** Representative images of tdTomato+ cells (red) and p-S6 staining (green) in mouse mPFC at P28-43. **(d)** Quantification of p-S6 staining intensity (normalized to the mean control) in tdTomato+ neurons. **(e)** Quantification of tdTomato+ neuron soma size. **(f)** Representative images of tdTomato+ neuron (red) placement and distribution in coronal mPFC sections. Red square on the diagram denotes the imaged area for all groups. CC, corpus callosum. **(g)** Quantification of tdTomato+ neuron placement in layer 2/3. Left diagram depicts the approach for analysis: the total number of tdTomato+ neurons within layer 2/3 (white square) was counted and expressed as a % of total neurons in the imaged area. Right bar graphs show the quantification. **(h)** Quantification of tdTomato+ neuron distribution across cortical layers. Left diagram depicts the approach for analysis: the imaged area was divided into 10 equal-sized bins across the cortex, spanning the corpus callosum to the pial surface (white grids); the total number of tdTomato+ neurons within each bin was counted and expressed as a % of total neurons in the imaged area. Right bar graphs show the quantification. For graphs **d, e**: n = 4-8 mice per group, with 6-15 cells analyzed per animal. For graphs **g, h**: n = 3-7 mice per group, with 1 brain section analyzed per animal. Statistical comparisons were performed using (**d, e**) nested one-way ANOVA (fitted to a mixed-effects model) to account for correlated data within individual animals, (**g**) one-way ANOVA, or (**h**) two-way repeated measures ANOVA. Post-hoc analyses were performed using Holm-Šídák multiple comparison test. *$p<0.05$, **$p<0.01$, ***$p<0.001$, ****$p<0.0001$. All data are reported as the mean of all neurons or brain sections in each group ± SEM.

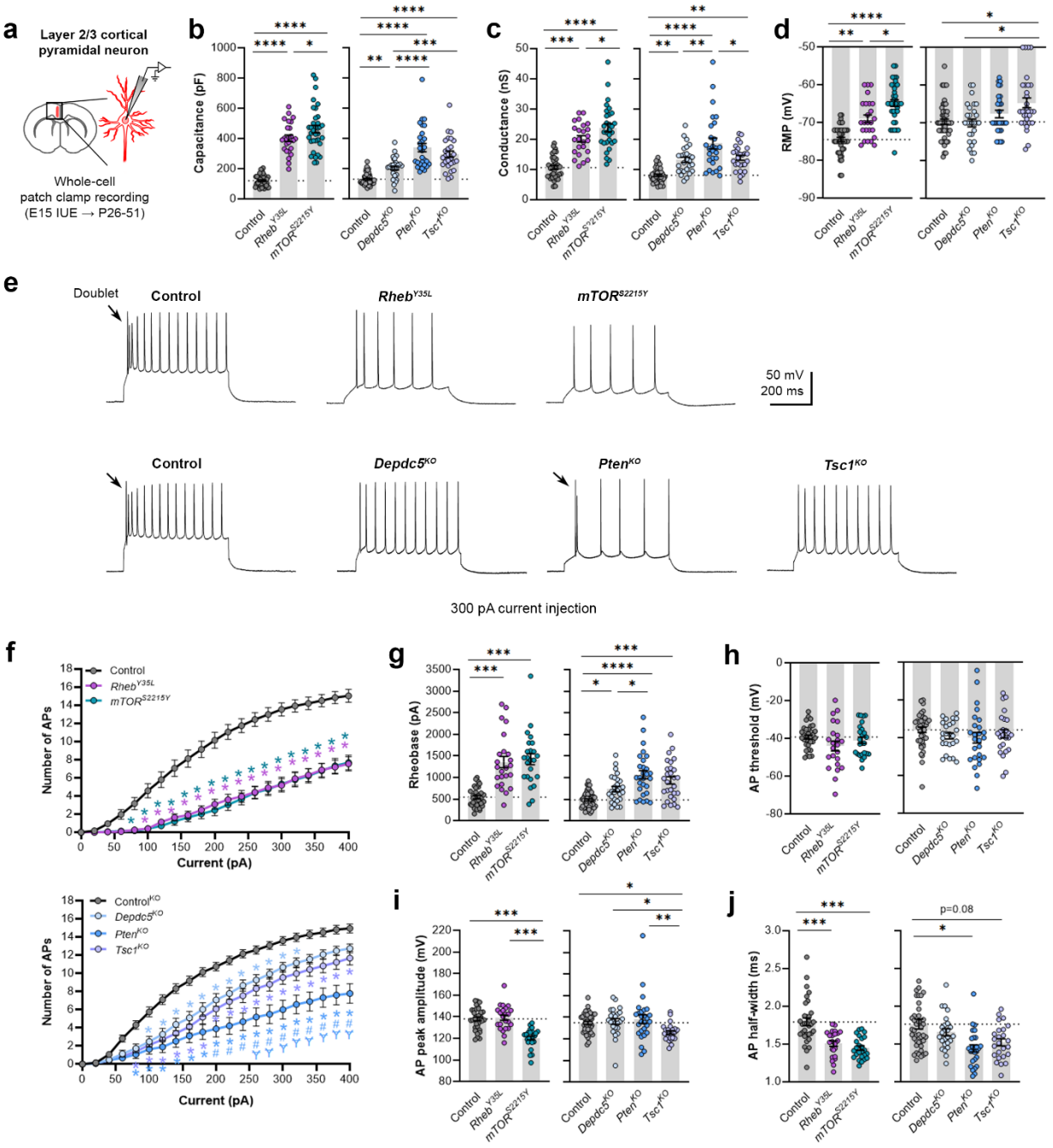
a
Layer 2/3 cortical pyramidal neuron
Whole-cell patch clamp recording (E15 IUE → P26-51)
b
Capacitance (pF)
c
Conductance (nS)
d
RMP (mV)
Control
Rheb Y35L
mTOR S2215Y
Depdc5 KO
Pten KO
Tsc1 KO
e
Doublet
Control
Rheb Y35L
mTOR S2215Y
50 mV
200 ms
Depdc5 KO
Pten KO
Tsc1 KO
300 pA current injection
f
Number of APs
Current (pA)
Control KO
g
Rheobase (pA)
h
AP threshold (mV)
i
AP peak amplitude (mV)
j
AP half-width (ms)
p=0.08

Figure 2: Expression of *Rheb*^{Y35L}, *mTOR*^{S2215Y}, *Dedpdc5*^{KO}, *Pten*^{KO}, and *Tsc1*^{KO} universally leads to decreased depolarization-induced excitability, but only *Rheb*^{Y35L}, *mTOR*^{S2215Y}, and *Tsc1*^{KO} expression leads to depolarized RMPs. (a) Diagram of experimental approach for whole-cell patch clamp recording. Recordings were performed in layer 2/3 pyramidal neurons in acute coronal slices from P26-51 mice, expressing either control, *Rheb*^{Y35L}, *mTOR*^{S2215Y}, *Dedpdc5*^{KO}, *Pten*^{KO}, or *Tsc1*^{KO} plasmids. **(b-d)** Graphs of membrane capacitance, resting membrane conductance, and RMP. **(e)** Representative traces of the AP firing response to a 300 pA depolarizing current injection. **(f)** Input-output curves showing the mean number of APs fired in response to 500 ms-long depolarizing current steps from 0 to 400 pA. Arrows point to initial spike doublets. **(g-j)** Graphs of rheobase, AP threshold, AP peak amplitude, and AP half-width. For **all** graphs: n = 5-10 mice per group, with 22-50 cells analyzed per animal. Statistical comparisons were performed using **(b-d, g-j)** nested one-way ANOVA (fitted to a mixed-effects model) to account for correlated data within individual animals or **(f)** mixed-effects ANOVA accounting for repeated measures. Post-hoc analyses were performed using Holm-Šídák multiple comparison test. *p<0.05, **p<0.01, ***p<0.001, ****p<0.0001, for the input-output curves in **f**: *p<0.05 (vs. control), #<0.05 (vs. *Dedpdc5*^{KO}), ϒp<0.05 (vs. *Tsc1*^{KO}). All data are reported as the mean of all neurons in each group ± SEM.

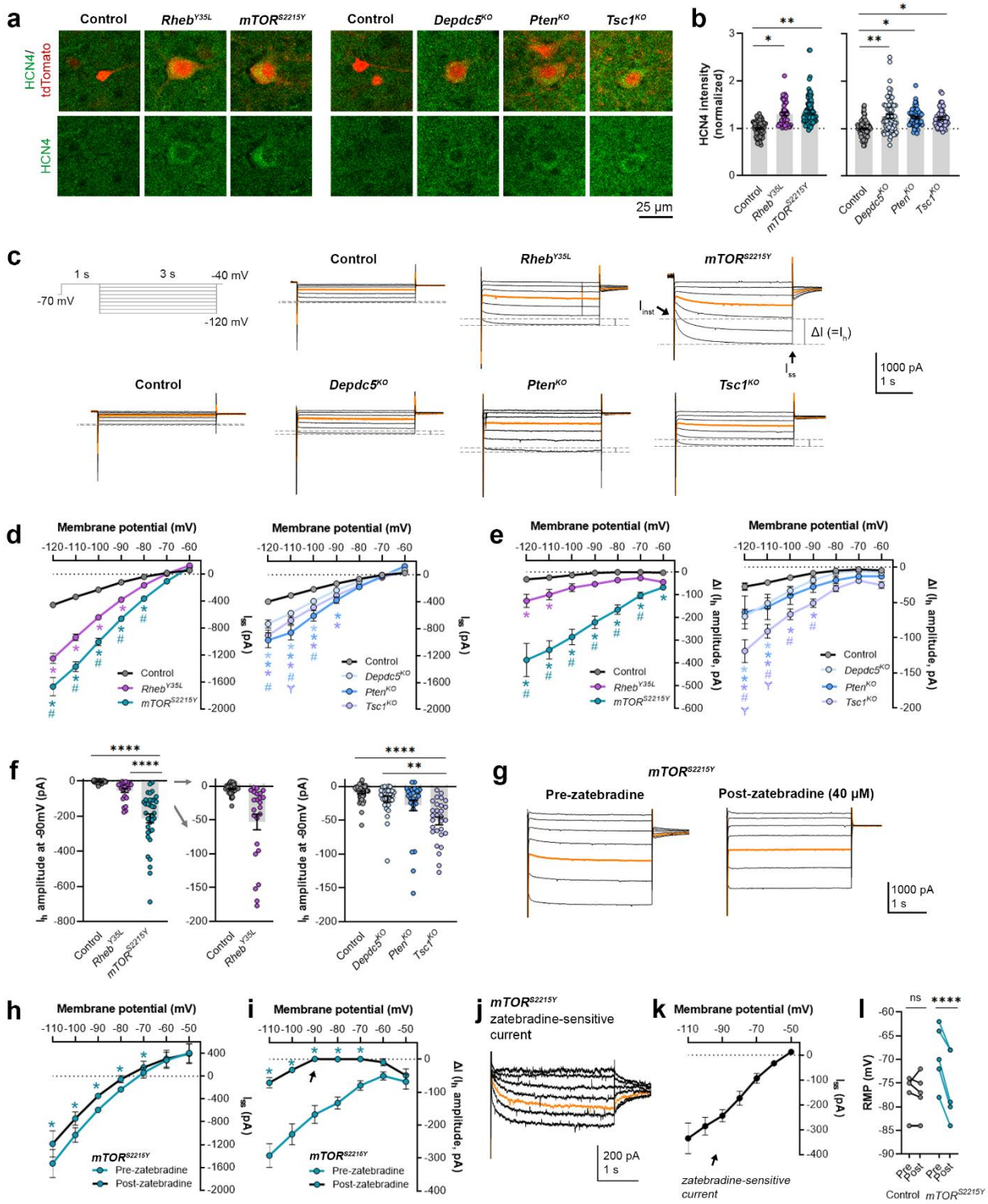
a
Control
Rheb Y35L
mTOR S2215Y
Control
Depdc5 KO
Pten KO
Tsc1 KO
HCN4/ tdTomato
HCN4
25 µm
b
HCN4 intensity (normalized)
Control
Rheb Y35L
mTOR S2215Y
Control
Depdc5 KO
Pten KO
Tsc1 KO
c
1 s
3 s
-40 mV
-70 mV
-120 mV
Control
Rheb Y35L
mTOR S2215Y
I inst
ΔI (=I h)
I ss
1000 pA
1 s
Control
Depdc5 KO
Pten KO
Tsc1 KO
d
Membrane potential (mV)
I ss (pA)
Control
Rheb Y35L
mTOR S2215Y
Depdc5 KO
Pten KO
Tsc1 KO
e
Membrane potential (mV)
ΔI (I h) amplitude, pA)
Control
Rheb Y35L
mTOR S2215Y
Depdc5 KO
Pten KO
Tsc1 KO
f
I h amplitude at -90mV (pA)
Control
Rheb Y35L
mTOR S2215Y
Control
Rheb Y35L
Control
Depdc5 KO
Pten KO
Tsc1 KO
g
mTOR S2215Y
Pre-zatebradine
Post-zatebradine (40 µM)
1000 pA
1 s
h
Membrane potential (mV)
I ss (pA)
mTOR S2215Y
Pre-zatebradine
Post-zatebradine
i
Membrane potential (mV)
ΔI (I h) amplitude, pA)
mTOR S2215Y
Pre-zatebradine
Post-zatebradine
j
mTOR S2215Y
zatebradine-sensitive current
200 pA
1 s
k
Membrane potential (mV)
I ss (pA)
zatebradine-sensitive current
l
ns
RMP (mV)
Pre
Post
Pre
Post
Control
mTOR S2215Y

Figure 3: Expression of *Rheb*^{Y35L}, *mTOR*^{S2215Y}, *Dedpdc5*^{KO}, *Pten*^{KO}, and *Tsc1*^{KO} leads to the abnormal presence of HCN4 channels with variations in functional expression. (a) Representative images of tdTomato+ cells (red) and HCN4 staining (green) in mouse mPFC at P28-43. **(b)** Quantification of HCN4 intensity (normalized to the mean control) in tdTomato+ neurons. **(c)** Representative current traces in response to a series of 3 s-long hyperpolarizing voltage steps from -120 to -40 mV, with a holding potential of -70 mV. Current traces from the -40 and -50 mV steps were not included due to contamination from unclamped Na+ spikes. Orange lines denote the current traces at -90 mV. **(d)** IV curve obtained from I_{ss} amplitudes. **(e)** ΔIV curve obtained from I_h amplitudes (i.e., ΔI, where $\Delta I = I_{ss} - I_{inst}$). **(f)** Graphs of I_h amplitudes at –90 mV. **(g)** Representative current traces in response to a series of 3-s long hyperpolarizing voltage steps from -110 mV to -50 mV in the *mTOR*^{S2215Y} condition pre- and post-zatebradine application. Orange lines denote the current traces at -90 mV. **(h)** IV curve obtained from I_{ss} amplitudes in the *mTOR*^{S2215Y} condition pre- and post-zatebradine application. **(i)** ΔIV curve obtained from I_h amplitudes (i.e., ΔI) in the *mTOR*^{S2215Y} condition pre- and post-zatebradine application. Arrow points to the post-zatebradine I_h amplitude at -90 mV. **(j)** Representative traces of the zatebradine-sensitive current obtained after subtraction of the post- from the pre-zatebradine current traces in response to -110 mV to -50 mV voltage steps. Orange lines denote the current traces at -90 mV. **(k)** IV curve of the zatebradine-sensitive current obtained after subtraction of the post- from the pre-zatebradine current traces. **(l)** Graph of RMP in the control and *mTOR*^{S2215Y} conditions pre- and post-zatebradine application. Connecting lines denote paired values from the same neuron. For graph **b**: n = 4-8 mice per group, with 4-15 cells analyzed per animal. For graphs **d, e, f**: n = 5-10 mice per group, with 24-47 cells analyzed per animal. For graphs **h, i, k, l**: n = 4-6 neurons (paired). Statistical comparisons were performed using (**b, f**) nested ANOVA (fitted to a mixed-effects model) to account for correlated data within individual animals, (**d, e)** mixed-effects ANOVA accounting for repeated measures, or (**h, i, l**) two-way repeated measures ANOVA. Post-hoc analyses were performed using Holm-Šídák multiple comparison test. *p<0.05, **p<0.01, ****p<0.0001, for the IV curves in **d, e, h, i**: *p<0.05 (vs. control), #p<0.05 (vs. *Rheb*^{Y35L} or *Dedpdc5*^{KO}), Ɏp<0.05 (vs. *Pten*^{KO}). All data are reported as the mean of all neurons in each group ± SEM.

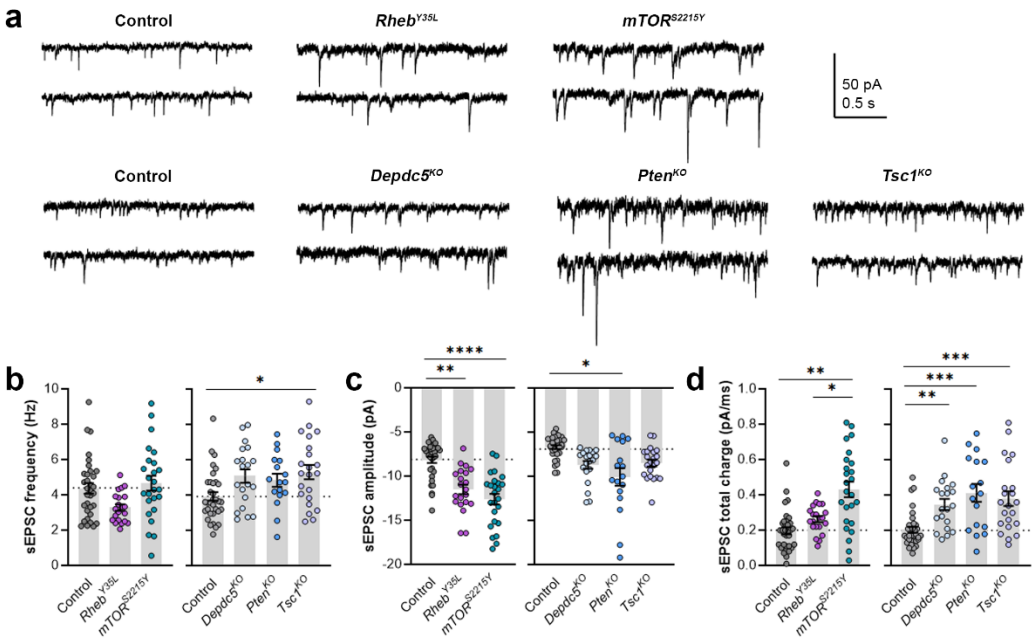

Figure 4: Expression of *Rheb*^{Y35L}, *mTOR*^{S2215Y}, *Dedpdc5*^{KO}, *Pten*^{KO}, and *Tsc1*^{KO} leads to different impacts on sEPSC properties. (a) Representative sEPSC traces recorded at a holding voltage of -70 mV. Top and bottom traces are from the same neuron. **(b-d)** Graphs of sEPSC frequency, amplitude, and total charge. For **all** graphs: n = 5-9 mice per group, with 17-34 cells analyzed per animal. Statistical comparisons were performed using a nested ANOVA (fitted to a mixed effects model) to account for correlated data within individual animals. Post-hoc analyses were performed using Holm-Šídák multiple comparison test. *p<0.05, **p<0.01, ***p<0.001, ****p<0.0001. All data are reported as the mean of all neurons in each group ± SEM.

Table 1: Statistical results (for main figures)

Fig. 1d: p-S6 INTENSITY

	Control	*Rheb*^{Y35L}	*mTOR*^{S2215Y}	Nested one-way ANOVA[a] F, DFn, DFd	p-value	Control	*Depdc5*^{KO}	*Pten*^{KO}	*Tsc1*^{KO}	Nested one-way ANOVA[a] F, DFn, DFd	p-value
Mean ± SD	1.00 ± 0.7	2.50 ± 0.7	1.84 ± 0.6	36.46, 2, 12	<0.0001	1.00 ± 0.5	2.04 ± 0.8	2.52 ± 0.5	2.17 ± 0.8	25.31, 3, 19	<0.0001
No. of animals	5	4	6			8	5	6	4		
No. cells/ animal	15	15 (6 for one mouse)	15			15	15	15 (8, 11 for two mice)	15		
Total cells	75	51	90			120	75	79	60		

Fig. 1e: NEURON SOMA SIZE

	Control	*Rheb*^{Y35L}	*mTOR*^{S2215Y}	Nested one-way ANOVA[a] F, DFn, DFd	p-value	Control	*Depdc5*^{KO}	*Pten*^{KO}	*Tsc1*^{KO}	Nested one-way ANOVA[a] F, DFn, DFd	p-value
Mean ± SD	84.3 ± 15.9	283.2 ± 86.4	294.8 ± 80.0	57.17, 2, 12	<0.0001	105.0 ± 21.0	174.7 ± 55.8	285.2 ± 90.8	222.6 ± 87.3	49.30, 3, 19	<0.0001
No. of animals	5	4	6			8	5	6	4		
No. cells/ animal	15	15 (6 for one mouse)	15			15	15	15 (8, 11 for two mice)	15		
Total cells	75	51	90			120	75	79	60		

Fig. 1f: NEURON POSITIONING (% cells in layer 2/3)

	Control	*Rheb*^{Y35L}	*mTOR*^{S2215Y}	One-way ANOVA F (DFn, DFd)	p-value	Control	*Depdc5*^{KO}	*Pten*^{KO}	*Tsc1*^{KO}	One-way ANOVA F (DFn, DFd)	p-value
Mean ± SD	82.7 ± 10.2	19.2 ± 12.6	31.6 ± 7.4	F (2, 11) = 55.09	<0.0001	87.6 ± 5.3	54.8 ± 11.7	80.6 ± 11.3	40.9 ± 10.8	F (3, 16) = 22.81	<0.0001
No. of animals	5	3	6			7	4	6	3		

Fig. 1h: NEURON POSITIONING (% cells in bins)

	No. of animals	Two-way repeated measures ANOVA	F (DFn, DFd)	p value		No. of animals	Two-way repeated measures ANOVA	F (DFn, DFd)	p value
Control	5	**Bin x Group**	F (18, 99) = 12.58	<0.0001	**Control**	7	**Bin x Group**	F (27, 144) = 5.802	<0.0001
Rheb^{Y35L}	3	**Bin**	F (9, 99) = 16.14	<0.0001	***Depdc5***^{KO}	4	**Bin**	F (9, 144) = 95.04	<0.0001
mTOR^{S2215Y}	6	**Group**	F (2, 11) = 0.3745	0.6961	***Pten***^{KO}	6	**Group**	F (3, 16) = 1.021	0.4095
					Tsc1^{KO}	3			

Fig. 2b: MEMBRANE CAPACITANCE (pF)

	Control	*Rheb*^{Y35L}	*mTOR*^{S2215Y}	Nested one-way ANOVA[a] F, DFn, DFd	p-value	Control	*Depdc5*^{KO}	*Pten*^{KO}	*Tsc1*^{KO}	Nested one-way ANOVA[a] F, DFn, DFd	p-value
Mean ± SD	121.6 ± 36.6	402.3 ± 105.4	462.4 ± 147.0	109.6, 2, 20	<0.0001	-130.8 ± 38.1	205.0 ± 69.4	340.0 ± 142.5	295.9 ± 109.2	37.77, 3, 127	<0.0001
No. of animals	10	5	8			10	5	6	8		
No. cells/ animal	1-7	4-8	1-7			3-8	4-8	1-8	1-5		
Total cells	43	25	35			48	28	28	27		

Fig. 2c: MEMBRANE CONDUCTANCE (nS)

				Nested one-way ANOVA[a]						Nested one-way ANOVA[a]	

	Control	*Rheb*^{Y35L}	*mTOR*^{S2215Y}	F, DFn, DFd	p-value	Control	*Depdc5*^{KO}	*Pten*^{KO}	*Tsc1*^{KO}	F, DFn, DFd	p-value
Mean ± SD	10.6 ± 3.8	20.1 ± 5.3	23.7 ± 7.4	33.58, 2, 18	<0.0001	8.0 ± 2.4	13.1 ± 4.5	18.6 ± 9.2	13.8 ± 4.1	17.83, 3, 25	<0.0001
No. of animals	8	5	8			10	5	6	8		
No. cells/ animal	3-6	4-8	1-6			3-8	4-8	1-8	1-5		
Total cells	34	24	30			47	27	27	28		

Fig. 2d: RMP (mV)

	Control	*Rheb*^{Y35L}	*mTOR*^{S2215Y}	Nested one-way ANOVA[a] F, DFn, DFd	p-value	Control	*Depdc5*^{KO}	*Pten*^{KO}	*Tsc1*^{KO}	Nested one-way ANOVA[a] F, DFn, DFd	p-value
Mean ± SD	-74.5 ± 3.8	-69.0 ± 5.1	-64.9 ± 5.3	24.20, 2, 20	<0.0001	-69.7 ± 5.0	-70.0 ± 5.3	-67.6 ± 5.3	-64.7 ± 7.3	4.292, 3, 25	0.0142
No. of animals	10	5	8			10	5	6	8		
No. cells/ animal	1-7	4-8	1-7			3-8	4-8	1-8	1-5		
Total cells	42	25	36			52	28	28	31		

Fig. 2f: AP INPUT-OUTPUT CURVE

	No. of neurons	Mixed-effects ANOVA Fixed effects (type III)	F (DFn, DFd)	p-value		No. of neurons	Mixed-effects ANOVA Fixed effects (type III)	F (DFn, DFd)	p-value
Control	36	**Current step**	F (20, 1657) = 263.4	<0.0001	**Control**	50	**Current step**	F (20, 2579) = 600.7	<0.0001
***Rheb*^{Y35L}**	22	**Group**	F (2, 83) = 39.60	<0.0001	***Depdc5*^{KO}**	27	**Group**	F (3, 129) = 22.84	<0.0001
***mTOR*^{S2215Y}**	28	**Current step x group**	F (40, 1657) = 22.84	<0.0001	***Pten*^{KO}**	28	**Current step x group**	F (60, 2579) = 14.66	<0.0001
					***Tsc1*^{KO}**	28			

Fig. 2g: RHEBOBASE (pA)

	Control	*Rheb*^{Y35L}	*mTOR*^{S2215Y}	Nested one-way ANOVA[a] F, DFn, DFd	p-value	Control	*Depdc5*^{KO}	*Pten*^{KO}	*Tsc1*^{KO}	Nested one-way ANOVA[a] F, DFn, DFd	p-value
Mean ± SD	544.4 ± 225.3	1356.0 ± 634.6	1422.0 ± 624.2	26.74, 2, 77	<0.0001	484.4 ± 180.1	737.3 ± 315.2	1071.0 ± 503.5	935.7 ± 444.4	16.84, 3, 25	<0.0001
No. of animals	7	5	6			10	5	6	8		
No. cells/ animal	4-6	4-7	1-7			3-7	4-7	1-8	1-5		
Total cells	32	24	24			50	27	28	28		

Fig. 2h: AP THRESHOLD (mV)

	Control	*Rheb*^{Y35L}	*mTOR*^{S2215Y}	Nested one-way ANOVA[a] F, DFn, DFd	p-value	Control	*Depdc5*^{KO}	*Pten*^{KO}	*Tsc1*^{KO}	Nested one-way ANOVA[a] F, DFn, DFd	p-value
Mean ± SD	-39.2 ± 6.3	-44.0 ± 12.3	-41.0 ± 8.4	1.937, 2, 78	0.1511	-35.8 ± 9.4	-39.0 ± 7.9	-40.0 ± 14.4	-37.9 ± 11.1	0.6587, 3, 25	0.5852
No. of animals	7	5	6			10	5	6	8		
No. cells/ animal	4-6	3-7	1-6			2-6	3-7	1-7	1-5		
Total cells	33	23	25			42	25	26	25		

Fig. 2i: AP PEAK AMPLITUDE (mV)

				Nested one-way ANOVA[a]						Nested one-way ANOVA[a]	

	Control	*Rheb*^{Y35L}	*mTOR*^{S2215Y}	F, DFn, DFd	p-value	Control	*Depdc5*^{KO}	*Pten*^{KO}	*Tsc1*^{KO}	F, DFn, DFd	p-value
Mean ± SD	138.1 ± 10.1	139.0 ± 11.6	120.3 ± 8.9	20.51, 2, 15	<0.0001	135.0 ± 9.1	136.1 ± 12.9	138.3 ± 21.1	126.1 ± 7.8	4.239, 3, 116	0.0070
No. of animals	7	5	6			10	5	6	8		
No. cells/ animal	4-6	3-7	1-6			2-6	3-7	1-7	1-5		
Total cells	33	23	25			43	25	27	25		

Fig. 2j: AP half-width (ms)

	Control	*Rheb*^{Y35L}	*mTOR*^{S2215Y}	Nested one-way ANOVA[a] F, DFn, DFd	p-value	Control	*Depdc5*^{KO}	*Pten*^{KO}	*Tsc1*^{KO}	Nested one-way ANOVA[a] F, DFn, DFd	p-value
Mean ± SD	1.79 ± 0.30	1.50 ± 0.18	1.44 ± 0.14	18.45, 2, 15	<0.0001	1.76 ± 0.43	1.65 ± 0.23	1.44 ± 0.24	1.52 ± 0.23	3.679, 3, 25	0.0254
No. of animals	7	5	6			10	5	6	8		
No. cells/ animal	4-6	3-7	1-6			2-6	3-7	1-7	1-5		
Total cells	33	23	25			43	25	27	25		

Fig. 3b: HCN4 INTENSITY

	Control	*Rheb*^{Y35L}	*mTOR*^{S2215Y}	Nested one-way ANOVA[a] F, DFn, DFd	p-value	Control	*Depdc5*^{KO}	*Pten*^{KO}	*Tsc1*^{KO}	Nested one-way ANOVA[a] F, DFn, DFd	p-value
Mean ± SD	1.00 ± 0.16	1.30 ± 0.25	1.36 ± 0.31	7.499, 2, 12	0.0077	1.00 ± 0.16	1.26 ± 0.36	1.24 ± 0.18	1.22 ± 0.20	6.579, 3, 18	0.0034
No. of animals	5	4	6			8	5	5	4		
No. cells/ animal	15 (10 for one mouse)	15 (4 for one mouse, 11 for one mouse)	15 (14 for on mouse)			15 (13 for one mouse)	15 (12 for two mice, 14 for one mouse)	15 (7 for one mouse)	15 (8 for one mouse)		
Total cells	70	45	89			118	68	67	53		

Fig. 3d: IV CURVE

	No. of neurons	Mixed-effects ANOVA Fixed effects (type III)	F (DFn, DFd)	p-value		No. of neurons	Mixed-effects ANOVA Fixed effects (type III)	F (DFn, DFd)	p-value
Control	42	**Voltage step**	F (6, 537) = 821.1	<0.0001	**Control**	47	**Voltage step**	F (6, 714) = 569.5	<0.0001
Rheb^{Y35L}	24	**Group**	F (2, 95) = 144.5	<0.0001	***Depdc5***^{KO}	28	**Group**	F (3, 126) = 20.08	<0.0001
mTOR^{S2215Y}	32	**Voltage step x group**	F (12, 537) = 92.68	<0.0001	***Pten***^{KO}	27	**Voltage step x group**	F (18, 714) = 22.98	<0.0001
					Tsc1^{KO}	28			

Fig. 3e: ΔIV CURVE

	No. of neurons	Mixed-effects ANOVA Fixed effects (type III)	F (DFn, DFd)	p-value		No. of neurons	Mixed-effects ANOVA Fixed effects (type III)	F (DFn, DFd)	p-value
Control	42	**Voltage step**	F (6, 537) = 83.01	<0.0001	**Control**	47	**Voltage step**	F (6, 720) = 78.95	<0.0001
Rheb^{Y35L}	24	**Group**	F (2, 95) = 61.77	<0.0001	***Depdc5***^{KO}	28	**Group**	F (3, 126) = 16.35	<0.0001
mTOR^{S2215Y}	32	**Voltage step x group**	F (12, 537) = 33.33	<0.0001	***Pten***^{KO}	27	**Voltage step x group**	F (18, 720) = 5.506	<0.0001
					Tsc1^{KO}	28			

Fig. 3f: I_h AMPLITUDE at -90 mV (pA)

	Control	*Rheb*^{Y35L}	*mTOR*^{S2215Y}	Nested one-way ANOVA[a] F, DFn, DFd	p-value	Control	*Depdc5*^{KO}	*Pten*^{KO}	*Tsc1*^{KO}	Nested one-way ANOVA[a] F, DFn, DFd	p-value
Mean ± SD	-4.4 ± 7.2	-53.1 ± 56.7	-212.9 ± 151.4	29.22, 2, 20	<0.0001	-8.7 ± 12.1	-18.6 ± 23.7	-28.0 ± 41.1	-51.2 ± 31.2	10.34, 3, 25	<0.0001
No. of animals	10	5	8			10	5	6	8		
No. cells/ animal	1-7	4-8	1-7			3-8	4-8	1-8	1-5		
Total cells	42	24	36			47	28	27	29		

Fig. 3h: IV CURVE (ZATERBADINE, *mTOR*^{S221})

	No. of neurons	Two-way repeated measures ANOVA	F (DFn, DFd)	p value
Pre-zatebradine	4	**Voltage step**	F (6, 18) = 19.45	<0.0001
Post-zatebradine	4	**Group**	F (1, 3) = 58.36	0.0047
		Voltage step x group	F (6, 18) = 27.54	<0.0001

Fig. 3i: ΔIV CURVE (ZATEBRADINE, *mTOR*^{S22515Y})

	No. of neurons	Two-way repeated measures ANOVA	F (DFn, DFd)	p value
Pre-zatebradine	4	**Voltage step**	F (6, 18) = 17.70	<0.0001
Post-zatebradine	4	**Group**	F (1, 3) = 49.57	=0.0059
		Voltage step x group	F (6, 18) = 13.65	<0.0001

Fig. 3l: RMP (mV; ZATERBADINE, *control, mTOR*^{S22515Y})

	No. of neurons	Two-way repeated measures ANOVA	F (DFn, DFd)	p value
Pre-zatebradine (control)	6	**Treatment**	F (1, 9) = 37.42	0.0002
Post-zatebradine (control)	6	**Group**	F (1, 9) = 2.747	0.1318
Pre-zatebradine (*mTOR*^{S22515Y})	4	**Treatment x group**	F (1, 9) = 33.83	0.0003
Post-zatebradine (*mTOR*^{S22515Y})	4			

Fig. 4b: sEPSC FREQUENCY (Hz)

	Control	*Rheb*^{Y35L}	*mTOR*^{S2215Y}	Nested one-way ANOVA[a] F, DFn, DFd	p-value	Control	*Depdc5*^{KO}	*Pten*^{KO}	*Tsc1*^{KO}	Nested one-way ANOVA[a] F, DFn, DFd	p-value
Mean ± SD	4.4 ± 1.7	3.3 ± 0.8	4.7 ± 2.1	2.550, 2, 15	0.1114	3.9 ± 1.4	5.1 ± 1.7	4.8 ± 1.5	5.3 ± 1.9	4.054, 3, 89	0.0095
No. of animals	7	5	6			9	5	5	8		
No. cells/ animal	3-6	4-5	2-7			2-5	2-6	3-4	1-4		
Total cells	33	21	25			34	20	17	22		

Fig. 4c: sEPSC AMPLITUDE (pA)

				Nested one-way ANOVA[a]						Nested one-way ANOVA[a]	

	Control	*Rheb*^{Y35L}	*mTOR*^{S2215Y}	F, DFn, DFd	p-value	Control	*Depdc5*^{KO}	*Pten*^{KO}	*Tsc1*^{KO}	F, DFn, DFd	p-value
Mean ± SD	-8.1 ± 2.1	-11.5 ± 2.5	-12.6 ± 3.0	19.20, 2, 15	<0.0001	-6.7 ± 1.3	-8.7 ± 1.9	-10.1 ± 4.1	-8.5 ± 1.8	4.280, 3, 23	0.0154
No. of animals	7	5	6			9	5	5	8		
No. cells/ animal	3-6	4-5	2-7			2-5	2-6	3-4	1-4		
Total cells	33	21	25			34	20	17	22		

Fig. 4d: sEPSC TOTAL CHARGE (pA/ms)

	Control	*Rheb*^{Y35L}	*mTOR*^{S2215Y}	Nested one-way ANOVA[a] F, DFn, DFd	p-value	Control	*Depdc5*^{KO}	*Pten*^{KO}	*Tsc1*^{KO}	Nested one-way ANOVA[a] F, DFn, DFd	p-value
Mean ± SD	0.20 ± 0.12	0.26 ± 0.08	0.43 ± 0.22	8.300, 2, 15	0.0037	0.20 ± 0.10	0.35 ± 0.14	0.41 ± 0.21	0.38 ± 0.20	9.273, 3, 89	<0.0001
No. of animals	7	5	6			9	5	5	8		
No. cells/ animal	3-6	4-5	2-7			2-5	2-6	3-4	1-4		
Total cells	33	21	25			34	20	17	22		

[a]The nested one-way ANOVA fits a mixed-effects model wherein the main factor is treated as a fixed factor and the nested factor is treated as a random factor.
[b]Post-hoc analyses were performed using Holm-Šídák multiple comparison test. Significant post-hoc results ($p<0.05$) are denoted with symbols (*, #, Ɏ) on the graphs, with the number of symbols 1-4 denoting the significant levels $p<0.05$, <0.01, <0.001, and <0.0001, respectively. For all two-way repeated measured and mixed-effects model ANOVA, all significant results ($p<0.05$) are denoted with one symbol regardless of the significant level for clearness on the graphs.

Table 2: Plasmid DNA information

Plasmid name	Plasmid source/generation
pCAG-tdTomato	Addgene plasmid #83029; this plasmid was previously generated by our lab
pCAG-GFP	Addgene plasmid #11150; deposited by Dr. Connie Cepko
pCAG-tagBFP	Gift from Dr. Joshua Breunig[64]
pCAG-*Rheb*^{Y35L}-T2A-tdTomato	The *Rheb* insert was synthesized and subcloned into a pCAG-Kir2.1Mut-T2A-tdTomato construct (Addgene plasmid #60644) via SmaI and BamHI sites, after excision of Kir2.1. ***Rheb* insert sequence:** NM_053075.3 (*mus musculus)*, mutation: Y35L
pCAG-*mTOR*^{S2215Y}	The *mTOR* insert was subcloned from a pcDNA3-FLAG-mTOR-SS2215Y construct (Addgene plasmid #69013) into a pCAG-tdTomato construct (Addgene plasmid #83029) via 5'AgeI and 3'NotI sites, after excision of tdTomato. ***mTOR* insert sequence:** NM_004958 (*homo sapiens)*, mutation: S2215Y
pX330-Control (i.e., pX330-empty)	Addgene plasmid #42230; deposited by Dr. Feng Zhang
pX330-*Depdc5*	Gift from Dr. Stéphanie Baulac. The gRNA sequence (gRNA1) was originally validated by Ribierre *et al*[26]. **gRNA sequence (5' to 3'):** GTCTGTGGTGATCACGC (17 nt) The gRNA targets exon 16 of *Dedpc5* (NM_001025426, *mus musculus)*, resulting in deleterious indels and inactivation of the gene
pX330-*Pten*	Addgene plasmid #59909; deposited by Dr. Tyler Jacks. The gRNA sequence (gRNA1) was originally validated by Xue *et* al[28]. **gRNA sequence (5' to 3'):** AGATCGTTAGCAGAAACAAA (20 nt) The gRNA targets *Pten* (NM_008960, *mus musculus)*, resulting in deleterious indels and inactivation of the gene
pX330-*Tsc1*	The gRNA sequence was synthesized based on published sequences[27] and subcloned into a pX330-empty vector. The specificity of the gRNA (gRMA T4) was originally described and validated by Lim *et al*,[27]. **gRNA sequence (5' to 3'):** CAGTGTGGAGGAGTCCAGCA (20 nt) The gRNA targets exon 3 of *Tsc1* (NM_001289575, *mus musculus)*, resulting in deleterious indels and inactivation of the gene

Table 3: Plasmid concentrations for control and experimental conditions

Group	Plasmid name	Plasmid concentration (µg/µl)[a]
Control (for *Rheb*^{Y35L} littermates)[b]	pCAG-tdTomato	3.5
Control (for *mTOR*^{S2215Y} littermates)[b]	pCAG-GFP	2.5
	pCAG-tdTomato	1.0
Rheb^{Y35L}	pCAG-Rheb^{Y35L}-T2A-tdTomato	2.5
	pCAG-GFP	1.0
mTOR^{S2215Y}	pCAG-mTOR^{S2215Y}	2.5
	pCAG-tdTomato	1.0
Control	pX330-Control	2.5
	pCAG-tdTomato	1.0
	pCAG-tagBFP[c]	0.5
Depdc5^{KO}	pX330-*Depdc5*	2.5
	pCAG-tdTomato	1.0
	pCAG-GFP[c]	0.5
Pten^{KO}	pX330-*Pten*	2.5
	pCAG-tdTomato	1.0
	pCAG-GFP[c]	0.5
Tsc1^{KO}	pX330-*Tsc1*	2.5
	pCAG-tdTomato	1.0
	pCAG-GFP[c]	0.5

[a]Working plasmid solutions were diluted in water and contained 0.03% Fast Green dye to visualize the injection. For each embryo, 1.5 µl of the plasmid mixture was injected into the right ventricle.
[b]Control groups for *Rheb*^{Y35L} and *mTOR*^{S2215Y} contained pCAG tdTomato and pCAG-GFP+pCAG-tdTomato, respectively, to distinguish between control and experimental animals for each litter. The total plasmid concentration was kept equal between the two control groups. No differences were observed between the two groups, and therefore, they were combined into one control group.
[c]Equal concentrations of pCAG-tagBFP and pCAG-GFP were added into the control and experimental (*Depdc5*^{KO}, *Pten*^{KO}, and *Tsc1*^{KO}) groups, respectively, to distinguish the control and experimental animals for each litter.

SUPPLEMENTAL FIGURES AND TABLES

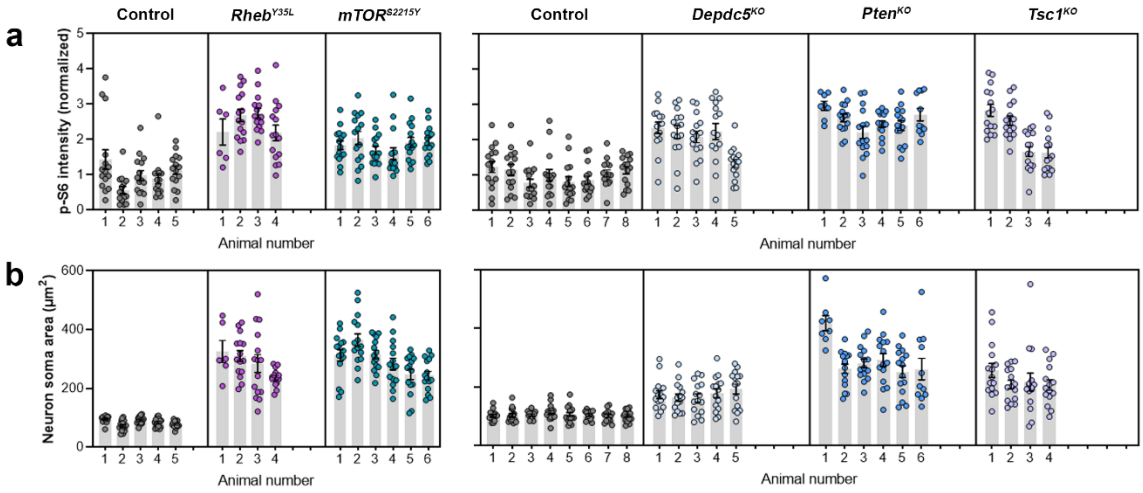

Figure S1: Distribution of p-S6 staining intensity and neuron soma size among individual animals P28-43. (a) Distribution of p-S6 staining intensity among individual animals. **(b)** Distribution of neuron soma size among individual animals.

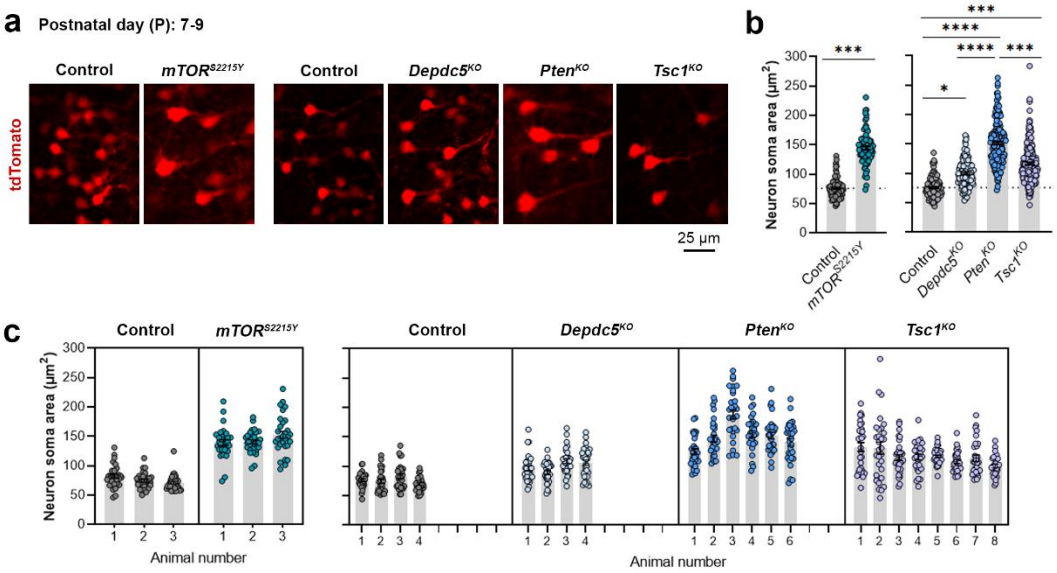

Figure S2: Neuron soma sizes at P7-9. (a) Representative images of tdTomato+ cells (red) in mouse mPFC at P7-9. **(b)** Quantification of tdTomato+ neuron soma size. **(c)** Graph showing the distribution of neuron soma size among individual animals in each group. n = 3-8 mice per group, with 30 cells analyzed per animal. Statistical comparisons were performed using a nested t-test (control vs. *mTOR*^{S2215Y}) or nested one-way ANOVA (control vs. *Dedpdc5*^{KO} vs. *Pten*^{KO}, vs. *Tsc1*^{KO}) (fitted to a mixed-effects model) to account for correlated data within individual animals. Post-hoc analyses were performed using Holm-Šídák multiple comparison test. *p<0.05, ***p<0.001, ****p<0.0001. Data are reported as the mean of all neurons in each group ± SEM.

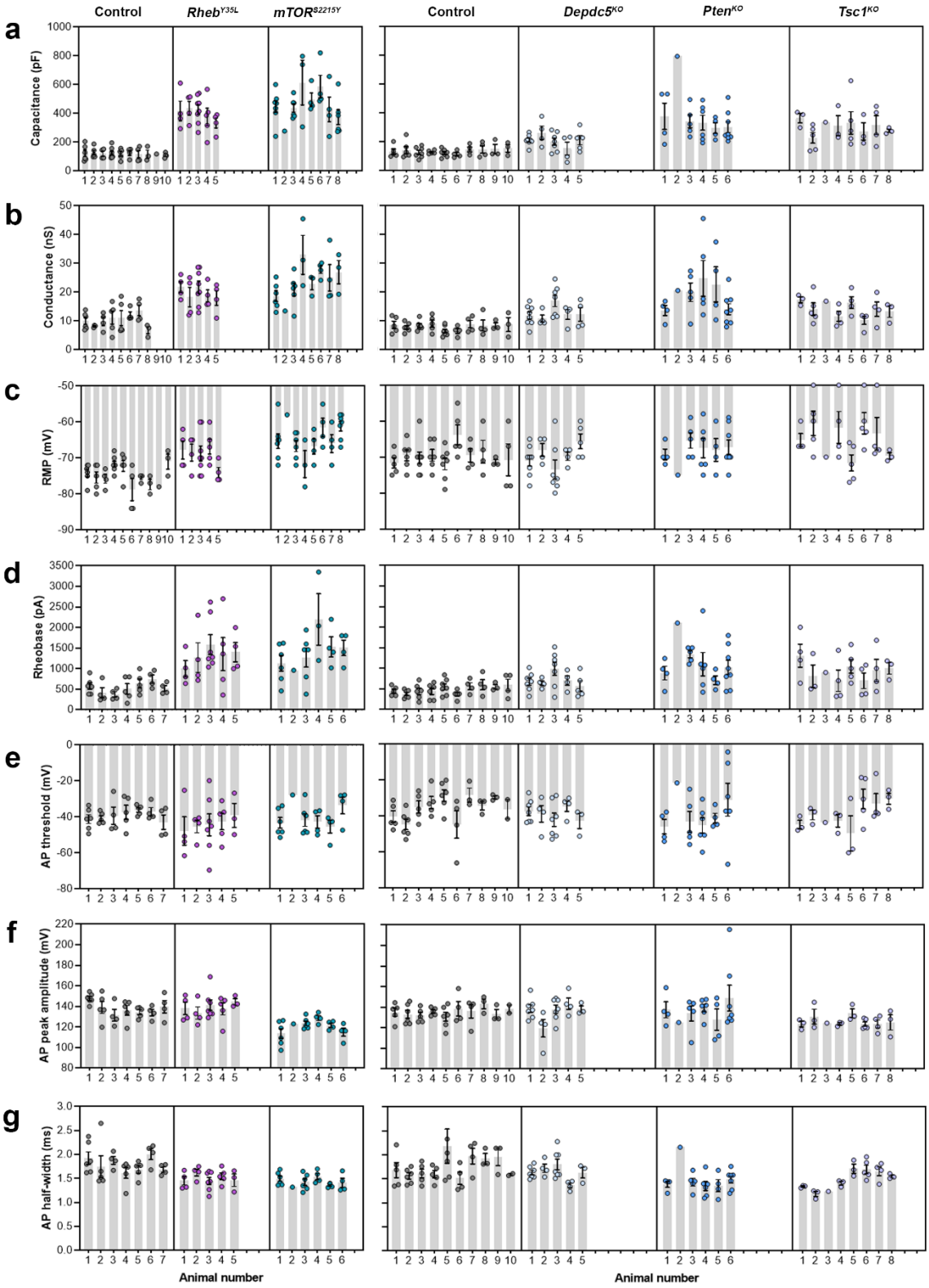

Figure S3: Distribution of membrane and AP properties among individual animals P26-51. (a-c) Distribution of membrane capacitance, conductance, and RMP among individual animals. (**d-g**) Distribution of rheobase, AP threshold, AP peak amplitude, and AP half-width among individual animals.

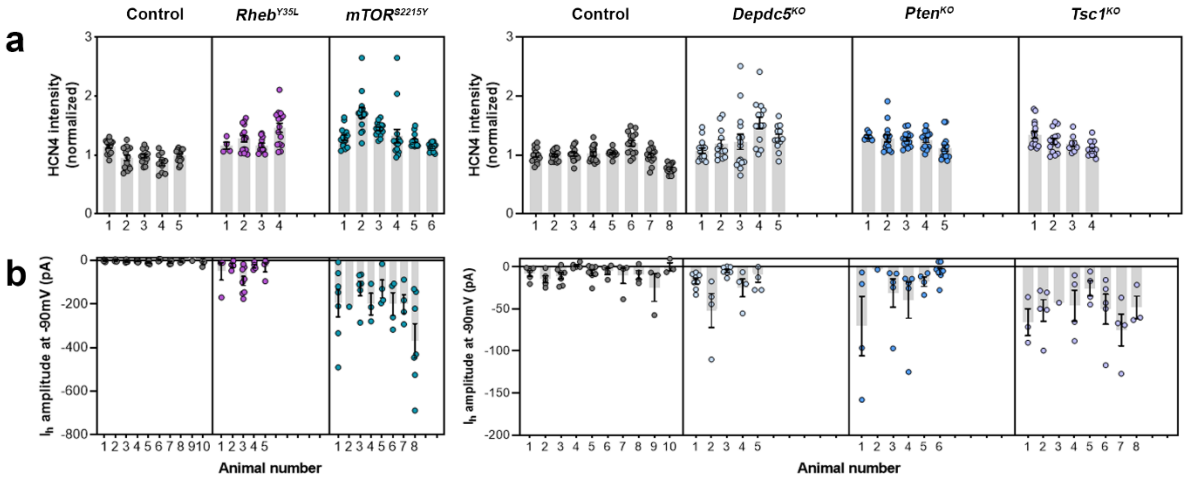

Figure S4: Distribution of HCN4 staining intensity and I_h amplitudes (at -90 mV) among individual animals at P28-43 and P26-51, respectively. (a) Distribution of HCN4 staining intensity among individual animals. (**d-g**) Distribution of I_h amplitudes (at -90 mV) among individual animals.

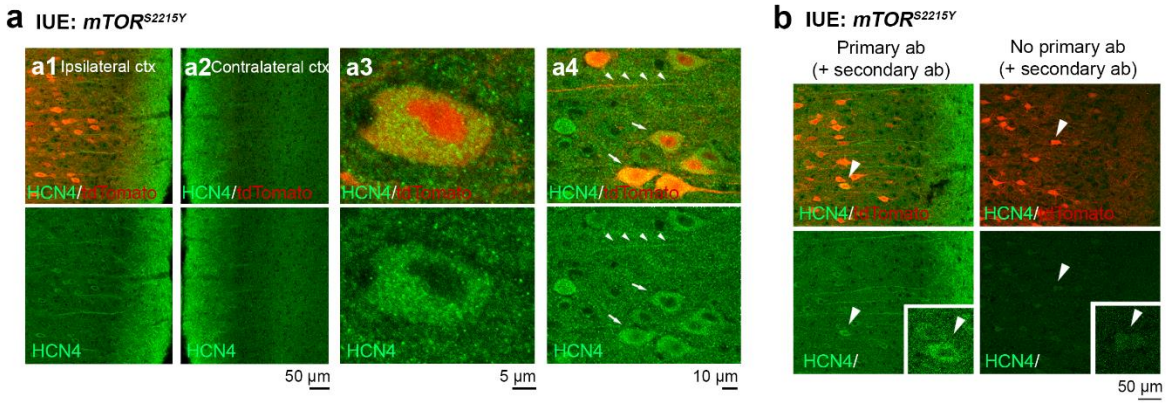

Figure S5: Additional images of HCN4 staining in mPFC sections from P28-43 mice expressing *mTOR*^{S2215Y}. (a) Representative images of tdTomato+ cells (red) and HCN4 staining (green). Top panels show overlay images. Bottom panels show HCN4 single-channel images. **a1** and **a2** show the ipsilateral and contralateral cortex, respectively. **a3** and **a4** are high-magnification images demonstrating HCN4 staining within the cell**. (b)** Representative images of immunostaining with (left) or without (right) HCN4 primary antibodies (control for secondary antibody specificity).

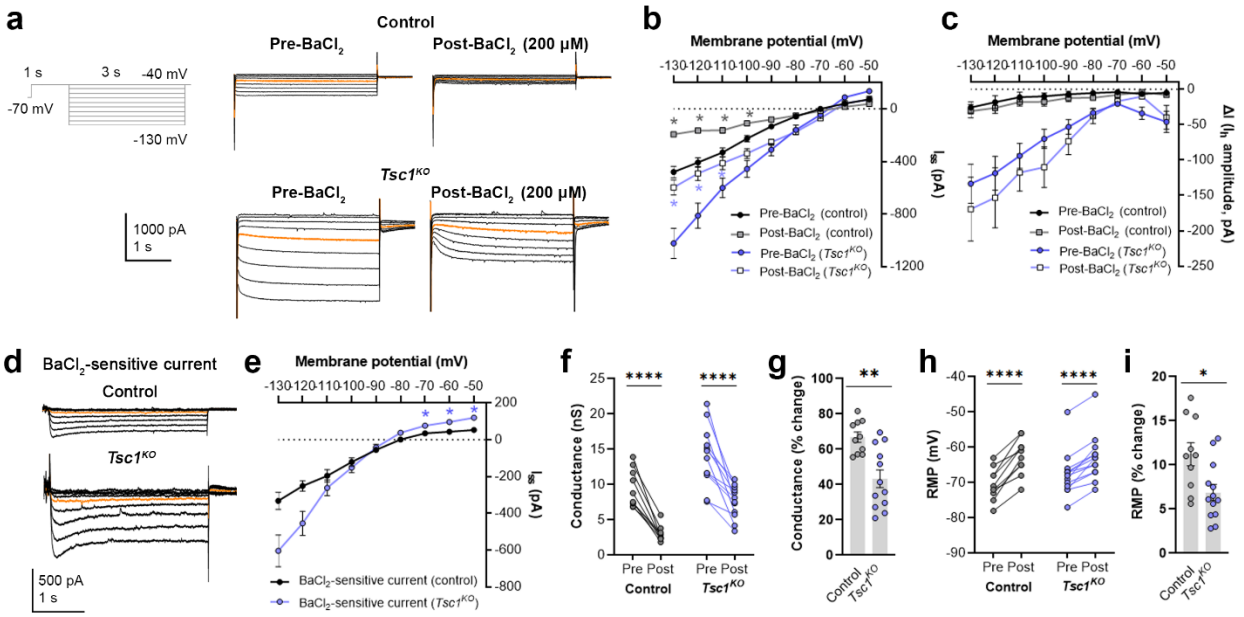

Figure S6: $BaCl_2$ application decreases overall inward currents without affecting I_h in *Tsc1^{KO}* neurons. **(a)** Representative current traces in response to a series of 3-s long hyperpolarizing voltage steps from -130 mV to -40 mV in the *Tsc1^{KO}* condition pre- and post-$BaCl_2$ application. Orange lines denote the current traces at -90 mV. **(b)** IV curve obtained from I_{ss} amplitudes in the *Tsc1^{KO}* condition pre- and post-$BaCl_2$ application. **(c)** IV curve obtained from I_h amplitudes (i.e., ΔI, where $\Delta I = I_{ss} - I_{inst}$) in the *Tsc1^{KO}* condition pre- and post-$BaCl_2$ application. **(d)** Representative traces of the $BaCl_2$-sensitive current obtained after subtraction of the post- from the pre-$BaCl_2$ current traces. Orange lines denote the current traces at -90 mV. **(e)** IV curve of the $BaCl_2$ -sensitive current obtained after subtraction of the post- from the pre- $BaCl_2$ current traces. The isolated $BaCl_2$-sensitive current reversed near -80 mV. **(f)** Graph of conductances (at -500 pA) in the control and *Tsc1^{KO}* conditions pre- and post-$BaCl_2$ application. Connecting lines denote paired values from the same neuron. **(g)** Graph of % change in conductances pre- and post-$BaCl_2$ application in the control and *Tsc1^{KO}* conditions. **(h)** Graph of RMP in the control and *Tsc1^{KO}* conditions pre- and post-$BaCl_2$ application. Connecting lines denote paired values from the same neuron. **(i)** Graph of % change in RMP pre- and post-$BaCl_2$ application in the control and *Tsc1^{KO}* conditions. For **all** graphs: n = 10-13 neurons per group. Statistical comparisons were performed using (**b, c, e**) mixed-effects ANOVA, (**f, h**) two-way repeated measures ANOVA, or (**g, i**) unpaired t-test. Post-hoc analyses were performed using Holm-Šídák multiple comparison test. *p<0.05, **p<0.01, ****p<0.0001. All data are reported as the mean of all neurons or brain sections in each group ± SEM.

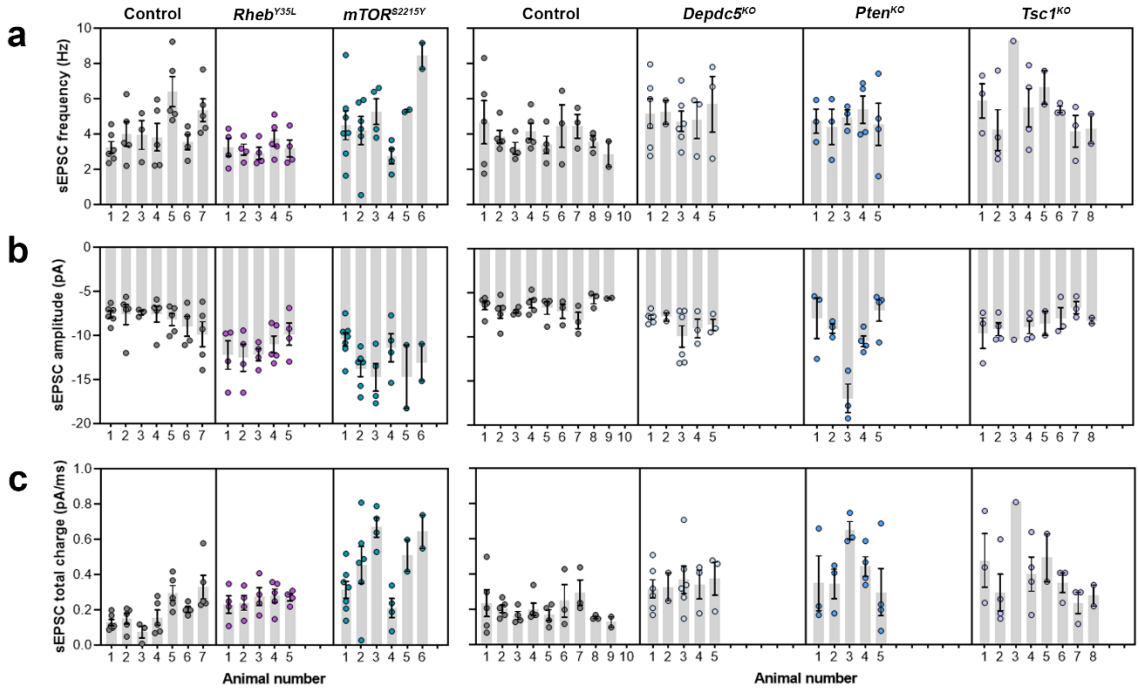

Figure S7: Distribution of sEPSC properties among individual animals at P26-51. (a-c) Distribution of sEPSC properties among individual animals.

Table S1: Statistical results (for supplemental figures)

Fig. S2b: NEURON SOMA SIZE (P7-9)

			Nested t-test[a]							Nested one-way ANOVA[a] *	
	Control	***mTOR^{S2215Y}***	**t, df**	**F, DFn, DFd**	**p-value**	**Control**	***Depdc5^{KO}***	***Pten^{KO}***	***Tsc1^{KO}***	**F, DFn, DFd**	**p-value**
Mean ± SD	76.2 ± 1.7	144.4 ±2.9	13.22, 4	174.8, 1, 4	0.0002	75.9 ± 1.5	100.1 ± 2.1	151.7 ± 2.8	116.7 ± 2.1	26.87, 3, 18	<0.0001
No. of animals	3	3				4	4	6	8		
No. cells/ animal	30	30				30	30	30	30		
Total cells	90	90				120	120	180	240		

Fig. S6b: IV CURVE ($BaCl_2$)

	No. of neurons	**Mixed-effects ANOVA** Fixed effects (type III)	**F (DFn, DFd)**	**p-value**	
Pre-$BaCl_2$ (control)	10	**Voltage step**	F (8, 72) = 201.6	<0.0001	
Post-$BaCl_2$ (control)	10	**Group**	F (1, 9) = 46.18	<0.0001	
		Voltage step x group	F (8, 55) = 45.52	<0.0001	
Pre $BaCl_2$ (*Tsc1^{KO}*)	13	**Voltage step**	F (8, 96) = 81.41	<0.0001	
Post-$BaCl_2$ (*Tsc1^{KO}*)	13	**Group**	F (1, 12) = 12.46	0.0041	
		Voltage step x group	F (8, 64) = 20.46	<0.0001	

Fig. S6c: ΔIV CURVE ($BaCl_2$)

	No. of neurons	**Mixed-effects ANOVA** Fixed effects (type III)	**F (DFn, DFd)**	**p-value**	
Pre-$BaCl_2$ (control)	10	**Voltage step**	F (8, 72) = 4.337	0.0003	
Post-$BaCl_2$ (control)	10	**Group**	F (1, 9) = 2.310	0.1629	
		Voltage step x group	F (8, 56) = 0.3825	0.9255	
Pre $BaCl_2$ (*Tsc1^{KO}*)	13	**Voltage step**	F (8, 96) = 12.53	<0.0001	
Post-$BaCl_2$ (*Tsc1^{KO}*)	13	**Group**	F (1, 12) = 0.7970	0.3895	
		Voltage step x group	F (8, 64) = 2.306	0.0307	

Fig. S6e: IV CURVE ($BaCl_2$-sensitive current)

	No. of neurons	**Mixed-effects ANOVA** Fixed effects (type III)	**F (DFn, DFd)**	**p-value**	
Control	10	**Voltage step**	F (1.252, 19.41) = 92.62	<0.0001	
Tsc1^{KO}	13	**Group**	F (1, 21) = 1.036	0.3204	
		Voltage step x group	F (8, 124) = 7.724	<0.0001	

Fig. S6f: CONDUCTANCE (nS, $BaCl_2$)

	No. of neurons	**Two-way repeated measures ANOVA**	**F (DFn, DFd)**	**p value**	
Control	10	**Group**	F (1, 20) = 20.04	0.0002	
Tsc1^{KO}	12	**Treatment**	F (1, 20) = 82.05	<0.0001	
		Group x treatment	F (1, 20) = 0.0002453	0.9877	

Fig. S6g: CONDUCTANCE (% change, $BaCl_2$)

	No. of neurons	**Unpaired t-test** t, df	**p-value**	
Control	10	t=3.841, df=20	0.0010	
Tsc1^{KO}	12			

Fig. S6h: RMP (mV, $BaCl_2$)

No. of neurons **Two-way repeated measures ANOVA**

			F (DFn, DFd)	p value	
Control	10	**Group**	F (1, 21) = 0.2692	0.6093	
Tsc1^{KO}	13	**Treatment**	F (1, 21) = 134.7	0.0001	
		Group x treatment	F (1, 21) = 9.281	0.0061	

Fig. S6i: RMP (% change, $BaCl_2$)

	No. of neurons	**Unpaired t-test**		
		t, df	**p-value**	
Control	10	t=2.810, df=21	0.0105	
Tsc1^{KO}	13			

[a]The nested t-test and ANOVA fit a mixed-effects model wherein the main factor is treated as a fixed factor and the nested factor is treated as a random factor.
[b]Post-hoc analyses were performed using Holm-Šídák multiple comparison test. Significant post-hoc results ($p<0.05$) are denoted with symbols (*) on the graphs, with the number of symbols 1-4 denoting the significant levels $p<0.05$, <0.01, <0.001, and <0.0001, respectively.